CHARACTERIZATION OF A MULTIMODE PROPELLANT OPERATING IN A POROUS GLASS ELECTROSPRAY THRUSTER

BY

ANTHONY ADDUCI

THESIS

Submitted in partial fulfillment of the requirements
for the degree of Master of Science in Aerospace Engineering
in the Graduate College of the
University of Illinois Urbana-Champaign, 2023

Urbana, Illinois

Adviser:

Professor Joshua L. Rovey

Abstract

Multimode space propulsion is an emerging technology that shows a promising increase in mission flexibility, adaptability, and mass savings for specific missions [1]. Finding a propellant that operates well in multiple propulsive modes is a key step in getting multimode propulsion systems flying in space. This study characterizes a novel multimode propellant named FAM-110A through operation in a porous glass electrospray thruster. Measurements acquired include current-voltage characteristic curves, plume ion potential via a retarding potential analyzer, and mass to charge ratio via a linear time of flight spectrometer. FAM-110A emitted more current at comparable emitter voltages as compared to EMIM-BF_4. Currents of 422 μA and 305 μA were observed at voltages of +1760 V and -1730 V respectively. RPA measurements showed less field free fragmentation during thruster operation with FAM-110A and also a 0.9% average energy efficiency. During cation emission, it was found that the FAM-110A plume consists of primarily the EMIM cation with no observable evidence of the presence of HA+. Many species were found to exist in the negative emission plume including the two know anions: nitrate, and ethylsulfate. Performance parameters were calculated for each propellant. The calculations showed the thruster operating with FAM-110A produced 3.9 μN and 9.1 μN more thrust in cation and anion emission, respectively. The specific impulse of FAM-110A was 1412 seconds lower in positive mode and 1485 seconds lower in negative mode. The calculated propulsive efficiency for FAM-110A was 35.9% lower during positive mode and 21.2% lower during negative mode when compared to EMIM-BF_4.

Acknowledgments

First I would like to thank my adviser, Dr. Rovey, for giving me the opportunity to continue my engineering education and conduct graduate level research within the Electric Propulsion Laboratory. Your support and guidance throughout my time at UIUC proved pivotal in my success. Thank you to all members of the EP Lab who I had the pleasure of working alongside. Bryan Cline, Avi Rao, and Allison Timm, thank you for being great friends along the way. I couldn't have asked for better people to spend all waking hours with working on coursework and research. Thank you to Chris Lyne for all of your help along the way and your profound knowledge in electrospray propulsion. Thank you to Dustin and Greg in the AE Machine shop for their knowledge, expertise, and willingness to converse with me on a daily basis about my project. Thank you to to my parents, Joe and Jill Adduci, for your never ending support and motivation. I would not be where I am today without you. Lastly, I would like to thank my fiancé Amanda for your unwavering support throughout my time in graduate school.

Table of contents

List of Symbols

ϵ_0	Permittivity of free space $\approx 8.85418782 \times 10^{-12}\, m^{-3} kg^{-1} s^4 A^2$.
E_n	Normal component of the electric field
P_i	Liquid internal pressure
γ	Surface tension
r_1, r_2	principal radii of curvature on liquid meniscus
β	Taylor cone half angle
r	Radial distance from Taylor cone apex
m	Mass
q	Charge expressed in terms of number of elementary charges ($1q \approx 1.602 \times 10^{-19}\, C$)
$\frac{m}{q}$	Mass to charge ratio expressed in amu/q
V_b	Unfragmented beam voltage
t	Time
L	Length of flight tube
V_{emit}	Emitter voltage
η_ϵ	Energy efficiency
η_{prop}	Porpulsive efficiency
I_{sp}	Specific impulse
T	Thrust
$\dot{m}$	Mass flow rate
g_0	Standard acceleration due to gravity on Earth ($g_0 \approx 9.81 m/s^2$)
T_{ToF}	Thrust calculated from ToF data
$\dot{m}_{ToF}$	Mass flow rate calculated from ToF data
I	Current
P_{in}	Input power

Chapter 1

Introduction

Multimode in-space propulsion consists of integrating two or more propulsive modes into a single system with a shared propellant. The sharing of propellant between propulsive modes introduces increased mass savings, enablement of new missions, and in situ mission adaptability [1]. Multimode propulsion systems typically integrate a high thrust chemical mode and a low thrust, high specific impulse electric mode to encapsulate a large mission space [2]. One promising chemical-electric multimode sytem being developed by the Electric Propulsion Laboratory at the University of Illinois Urbana-Champaign consists of a high specific impulse electrospray thruster, and a high thrust chemical monopropellant thruster. The main challenge in the development of a chemical-electric multimode propulsion system is finding a propellant that is suitable for both propulsive modes. A novel green ionic liquid propellant named FAM-110A has been developed by Froberg Aerospace LLC to address the the primary needs of a chemical-electric multimode system. FAM-110A consists of 59% Hydroxylammonium Nitrate (HAN), and 41% Ethyl-3-methylimidazolium ethyl-sulfate (EMIM-EtSO4) by mass [3]. The chemical decomposition of FAM-110A has been demonstrated by Rovey and Berg in a platinum microtube [4], and by Sharma et al. in a platinum catalyst microthruster [5]. In addition to chemical operation, stable electrospray operation of FAM-110A was demonstrated by Rovey and Berg [6], Wainwright et al. [7],[8], and Lyne et al. [3] in a capillary emitter configuration. The performance of this propellant in both modes is important for its success in a multimode space propulsion system.

An electrospray thruster operates by extracting and accelerating charged particles (ions or droplets) with electrostatic fields to generate thrust. Charged particles are extracted from an ionic liquid by applying an electric field between the emitter tip and a downstream extractor electrode. The electric field generates electrical stress at the fluid vacuum interface creating an imbalance between the surface tension of the liquid

and the electrostatic force. This imbalance leads to the deformation of the liquid meniscus into a conical shape known as a Taylor cone.

Mathematically, the Taylor cone follows from a pressure balance at the fluid-dielectric interface [9]. Here the fluid is assumed as a perfect conductor, so only the normal component of the electric field is considered.

$$\frac{1}{2}\epsilon_0 E_n^2 + P_i = \gamma\left(\frac{1}{r_1} + \frac{1}{r_2}\right) \tag{1.1}$$

Where E_n is normal component of the electric field, γ is the liquid surface tension, r_1 and r_2 are the principal radii of curvature at each point on the meniscus, P_i is the internal pressure, and ϵ_0 is the permittivity of free space. In a passive propellant feed system, the internal pressure can be assumed negligible ($P_i = 0$). At any point on the surface of a cone, the curvature radii can be expressed as [10]

$$r_1 = \frac{\cot\beta}{r} \tag{1.2}$$

where β is the cone half angle, and r is the radial distance from the cone apex. The second principle radius of curvature goes to infinity on the surface of a cone [10], $r_2 \to \infty$, so the pressure balance becomes:

$$\frac{1}{2}\epsilon_0 E_n^2 = \frac{\cot\beta}{r} \tag{1.3}$$

By assuming equipotentiality in equation 1.1, a conical solution is produced with a cone half angle of 49.3°. Although this gives a theoretical cone half angle during the electrospray process, observed Taylor cone half angles can differ from this value [10]. This can be due to non-negligible internal liquid pressure, breakdown of the assumption that the liquid is a perfect conductor, and space charge effects of the emitted particles. Instability arises when the electric field is strong enough such that the electrical pressure exceeds the surface tension of the liquid leading to charged particle emission. The potential required to induce this instability is known as the onset voltage.

There are three primary emitter configurations used in electrospray propulsion research: capillary, externally wetted, and porous. A diagram of each configuration can be found in Figure 1.1. In a capillary configuration, fluid is transported in a pressurized system via small closed tubes from the reservoir to the exit channel. Taylor cone formation and charge particle emission is concentrated to the exposed liquid at the exit [9]. Capillary emitter configurations have been widely used in research [7],[8],[3], and were successfully

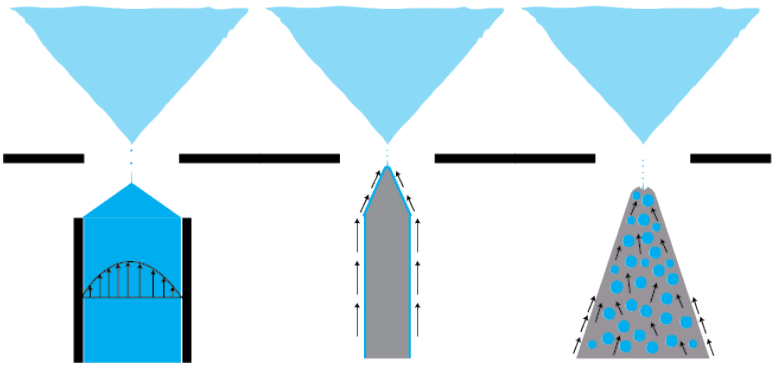

Figure 1.1: Diagram of commonly used electrospray emitter configurations. From left to right: capillary, externally wetted, porous.

demonstrated aboard LISA Pathfinder. The active propellant feed system required to operate a capillary electrospray device introduces increased complexity and mass into the system. Capillary configurations are also prone to clogging and the formation of bubbles within the transport tubes which can lead to changes in the operation.

In an externally wetted configuration, liquid is placed along the external surface of a solid emitter. The liquid wicks along the emitter surface until it reaches the tip of the structure. When an electric field is applied, Taylor cone formation and charged particle emission occurs at the tip. Externally wetted emitter configurations offer a simple electropsray device, however liquid selection becomes more important as full exposure to the low pressure operating environment excludes liquids with a non-negligible vapor pressure [9].

In a porous emitter configuration (the configuration of interest in this paper), a porous material is etched into a conical structure. Liquid wicks through the pores of the material towards the sharp tip and charged particles are then emitted from the pours when an electric field is applied. Porous emitter configurations are particulary advantages as they enable simple capillary driven, zero gravity compatible passive feeding of propellant [11]. This could reduce the mass, power, and volume requirements of a thruster by eliminating feed system components. A porous glass thruster can also operate in a bipolar mode, switching the polarity of the emitter voltage, enabling operation without the use of an external neutralizer.

Stable operation of a porous glass electrospray thruster has been demonstrated by Ma and Ryan [12] in the PET-100 thruster developed at University of Southampton. The PET-100 and other works investigating porous electrospray thrusters [11], demonstrate highly ionic emission using the ionic liquid EMIM-BF_4. Ma and Ryan also did a mission performance evaluation of the PET-100 thruster [10] demonstrating relatively high specific impulse, ranging from 3500 to 7500 seconds and a wide range of thrust from sub-μN to more than 260 μN. Natisin et al. developed a fully conventially machined, high performance porous glass electrospray thruster and characterized its performance operating with 1-Ethyl-3-methylimidazolium tetrafluoroborate

(EMIM-BF_4) [13]. The thruster operated successfully at emission currents up to $\pm$700 μA at applied emitter voltages of +1845 V and -1835 V for cation and anion emission, respectively. The fraction of the total current intercepted by the extractor grid was below 1% at emission currents up to 500 μA in positive mode and -700 μA in negative mode. Courtney et al. [11] compared direct and indirect thrust measurements of a porous glass electrospray configuration operating with different propellants. Thrusts up to $50\mu N$ were measured when operating with 1-ethyl-3-methylimidazolium-bis(trifluoromethylsulfonyl)imide in a bipolar mode at less than 0.8 W input power.

This paper investigates the electrospray performance and plume characteristics of the FAM-110A propellant through operation in a porous glass electrospray thruster manufactured at University of Illinois Urbana-Champaign. Current-voltage charactertistic curves are measured for both FAM-110A and EMIM-BF_4. A retarding potential analyzer is used to measure the energy of the beam, and time of flight spectrometry is used to determine the plume composition of FAM-110A propellant. This characterization will assess the propellants viability as a candidate for use in a multimode space propulsion system that consists of a chemical monopropellant thruster and porous glass electrospray thruster. The remainder of this paper is laid out as follows: an overview of the thruster design and fabrication, the experimental set up and a summary of the diagnostics used, results from thruster testing, discussion of the results, and conclusions drawn from this test campaign.

Chapter 2

Thruster Overview

2.1 Thruster Design and Fabrication

The thruster described here was fabricated and tested in the Electric Propulsion Laboratory at the University of Illinois Urbana-Champaign. The thruster design is based on the Air Force Electrospray Thruster Series 2 (AFET-2) [13], which was proposed as a high performance conventionally machined porous-media electrospray thruster to enable more wide spread research on this technology. An exploded view of the thruster components can be found in Figure 2.1. The AFET-2 is comprised of an exterior housing, an emitter housing, a disc spring, a porous borosilicate glass reservoir, a filter paper interface, a porous borosilicate glass emitter array, a distal electrode, a high voltage connection, and an extractor grid. There are four set screws at the bottom of the housing that move vertically to adjust the emitter height. There are eight set screws, two at each corner, around the perimeter of the extractor grid for x and y plane translation. The emitter array consists of 576 emitter structures machined from P5 grade porous borosilicate glass. The extractor grid is a two piece design; the aperture array is machined into a $76\mu m$ thick piece of molybdenum then bonded to a 0.76 mm molybdenum frame.

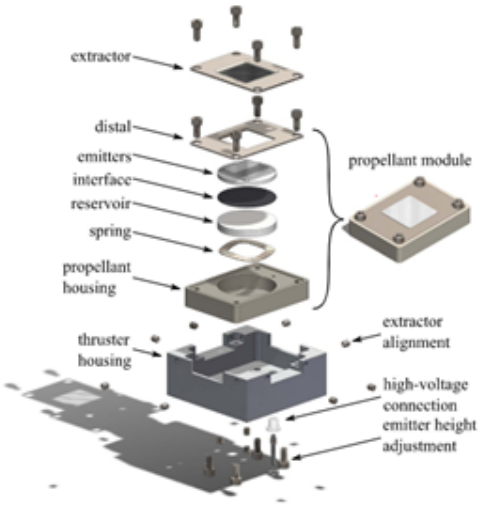

Figure 2.1: Thruster exploded view from [13]

The machining process described by Natisin et al. involved cutting the porous borosilicate glass, and the 76μm thick molybdenum extractor grid using aluminum titanium nitride (AlTiN) tools at a spindle speed of 50,000 rpm [13]. Modifications were made to the materials used for the extractor grid, and different fabrication processes of both the extractor and porous glass emitter array were explored.

2.1.1 Extractor Grid Fabrication

The extractor grid used in the UIUC thruster was fabricated using an RMI EF-20 laser engraver. 0.004 inch thick aluminum was chosen for the aperture array due to ease of use in the laser etching process. 0.76 mm thick stainless steel was chosen for the extractor frame. The frame was fabricated using a conventional mill. To fabricate the aperture array, the aluminum was bonded to a glass plate to ensure flatness was maintained throughout the engraving and bonding process. The aperture array pattern was then laser engraved into the stock aluminum. After the laser engraving process, the aperture array was left bonded to glass fixture. The extractor frame was then bonded to the aluminum using a silver conductive epoxy, and the completed extractor was debonded from the plate. After fabrication, the extractor aperture diameter and pitch were measured using a confocal microscope. The extractor grid had an average aperture diameter of 456μm and an average pitch of 547μm.

2.1.2 Emitter Array Fabrication

All of the manufactured emitter arrays described in this section were fabricated by the UIUC Aerospace Engineering Machine Shop. Emitter characterization was done using a Keyence VK-X1000 3D Optical

Profiler. CNC milling, laser ablation, and grinding were explored as possible manufacturing techniques for porous borosillicate glass electrospray emitter arrays. The substrate used in all techniques was a P5 porous borosilicate glass disk manufactured by ROBU with a diameter and thickness of 20 and 2.5 mm respectively.

CNC Milled Emitter Arrays

The first manufacturing technique explored was CNC milling. This technique follows directly from Natisin et al. [13]. It was reported that emitter height, radius of curvature, and emitter pitch of $300\mu m$, $10-20\mu m$, and $546\mu m$ respectively were achieved through conventional CNC machining at a spindle speed of 50,000 rpm. Milling at a lower spindle speed of 5,000 rpm was carried out. A height map, and image of the CNC milled emitter array is shown in Figure 2.2.

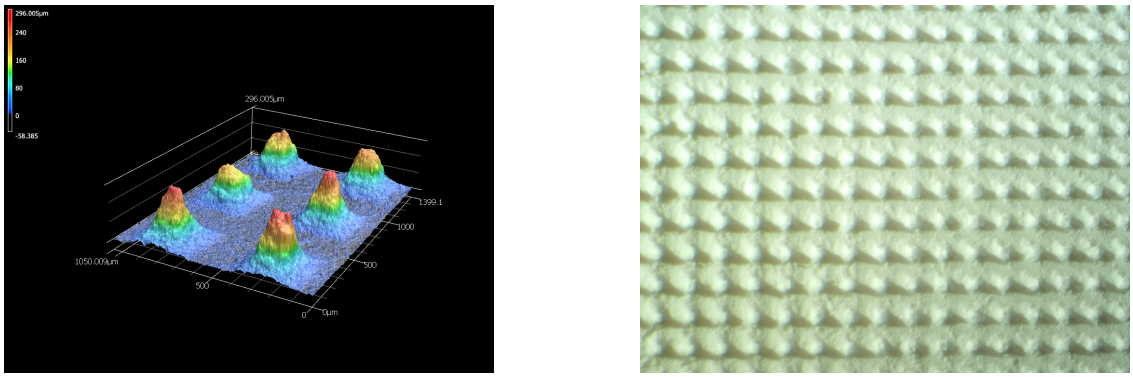

(a) 3D height map of a CNC milled emitter array

(b) Fabricated emitter array

Figure 2.2: CNC milled porous glass emitter array

The machining steps follow directly from Natisin [13]. An emitter platform is machined into the glass using a conventional mill. This platform serves to lock the emitter array within the thruster assembly by fixing the rotation. The platform also allows the emitter to be located above the top plane of the distal electrode. A second platform is machined along the perimeter of the emitter platform to ensure there are no partially formed emitter structures at the edges of the array. With the platforms machined, the end mill is then passed through the glass substrate following the tool path presented in [13]. The final step in the process is to rotate the tool path 90° and repeat the previous step machining an array of discrete emitter structures.

The CNC machined emitters have a mean height of $172 \pm 45\mu m$ and a mean radius of curvature of $63 \pm 34\mu m$. Non-uniformity in the geometry of the emitters is due to the low spindle speed during the manufacturing process. Natisin et al. found that higher speeds leads to sharper and more uniform emitter geometries [13]. Despite the poor geometry of the CNC machined emitters, it was still possible to successfully operate the electrospray thruster using the low speed CNC milled emitter arrays. These results are presented and discussed in a future section.

Laser Ablated Emitter Arrays

Laser ablation was chosen as another possible fabrication technique. Laser ablation was carried out on an Epilog Mini 24 Laser Cutter. The laser cutter is equipped with a 60-watt CO2 laser, and has a cutting area of 24" x 12" with a maximum resolution of 1200 DPI. Laser cutters have never before been used for laser ablation manufacturing techniques to make porous glass emitter arrays. A series of tests were conducted to determine the optimal laser settings for the ablation process. The four settings of interest included laser power, rasterisation speed, laser line width, and the number of passes. Laser power variation was tested by fixing the rasterisation speed at 50% and increasing the power from 20% to 100% in increments of 20%. Rasterisation speed variation was tested by fixing the laser power at 50% and increasing the rasterisation speed from 20% to 100% in increments of 20%. It was found that the degree of ablation increased with increasing power and decreasing rasterisation speed. Laser line width variation was tested by fixing both the power and rasterisation speed at 50%, and using four different line width settings: 0.13 mm, 0.18 mm, 0.25 mm, and 0.35 mm. To test the effect of the number of laser passes, the power and rasterisation speed were fixed at 50%, and the number of passes was varied from one to five. It was found that each pass was capable of ablating approximately $60\mu m$ of material at these fixed power and rasterisation settings. It was observed that exceeding three passes led to discoloration of the material with the discoloration intensifying with each increasing pass. After testing various settings combinations, it was determined that the optimal settings were 0.35 mm line width, 100% power, 30% rasterisation speed, and a laser pass count of 3. Figure 2.3 shows an image of a full emitter array fabricated using this technique.

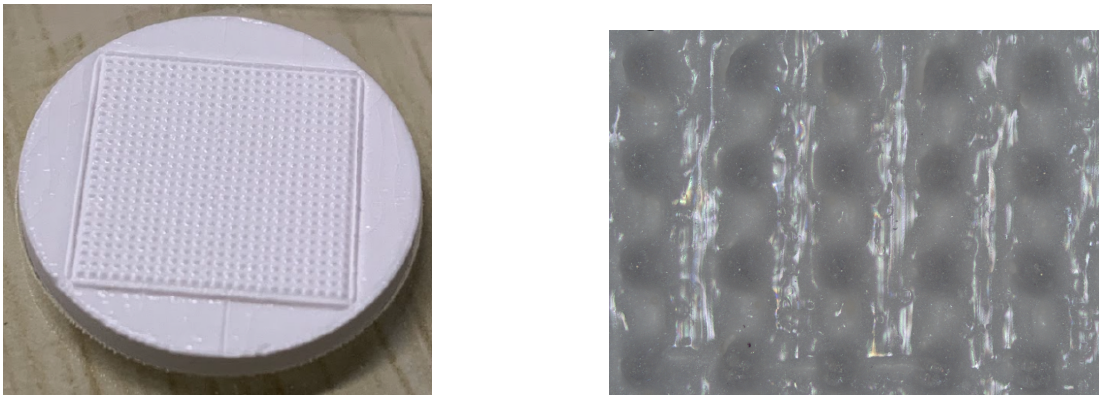

(a) **(b)**

Figure 2.3: (a) Image of full emitter array manufactured through laser ablation and (b) 5x optical image of emitter surface showing substrate melting.

Optical profiler measurements showed a mean emitter height of 210 μm, mean radius of curvature of 50 μm, and mean aspect ratio of 0.82. As compared to the geometry of the low speed CNC machined emitter

arrays, the laser ablation process was an improvement. The principle challenge however, was managing the heat load on the glass substrate. As seen in Figure 2.3a, the laser melted the top layer of glass creating a reflective surface and closing up the pores. Because of this, the thruster was unable to operate using the laser ablated emitter arrays.

Grinding Wheel Fabricated Emitter Arrays

The third manufacturing technique explored was grinding. Completed steps in the process for fabricating the ground emitter array is shown in Figure 2.4. Grinding was chosen as an alternate approach to emitter array manufacturing due to its simplicity and cost effectiveness. The first step follows directly from Natisin et al. [13]. An emitter platform is machined into the glass using a conventional mill. This platform serves to lock the emitter array within the thruster assembly by fixing the rotation. The platform also allows the emitter to be located above the top plane of the distal electrode. A second platform is machined along the perimeter of the emitter platform to ensure there are no partially formed emitter structures at the edges of the array.

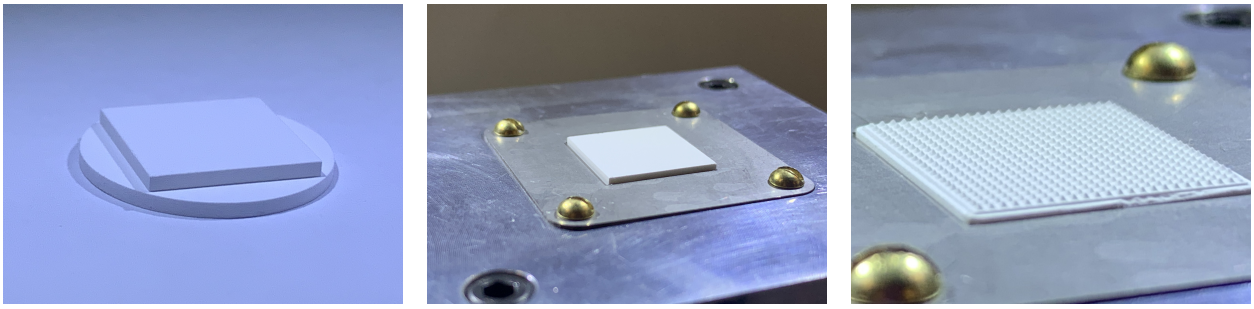

(a) Machined Emitter Platform **(b)** Substrate Clamped in Fixture **(c)** Machined Emitter Array

Figure 2.4: Porous Glass Emitter Fabrication Process

The fabrication of the emitter structures was done using a custom diamond edge grinding wheel manufactured by Norton Abrasives. The wheel edge has a base length of 0.015 inches and is angled 15°. Prior to fabrication, a fixture was manufactured to clamp the glass substrate in place, and allow for accurate angular indexing. With the substrate fixed in place, the fixture angle must be properly zeroed and the grinding wheel set to the correct x, y, and z locations. The grinding wheel then performs a series of linear passes in the x direction creating long continues structures in each row. The fixture is then indexed 90° and the process is repeated. The final product is a 24x24 array of discrete pyramidal emitter structures show in Figure 2.5.

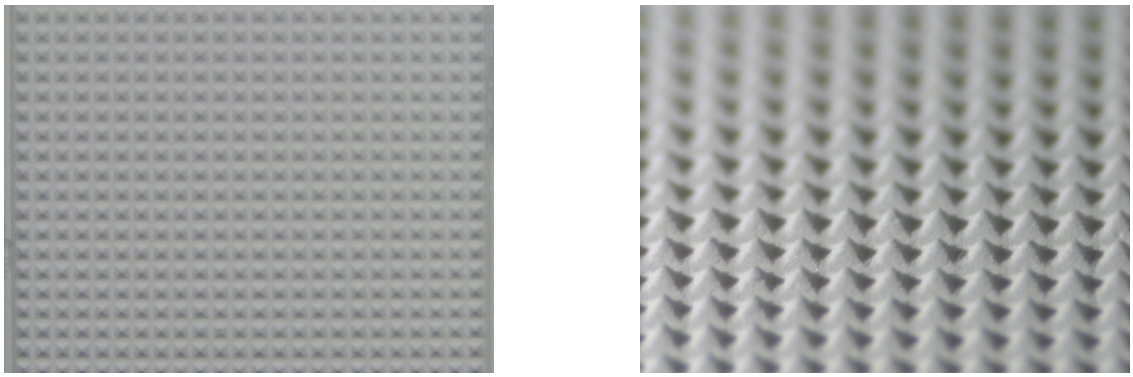

(a) Ground Emitter Array Top View **(b)** Ground Emitter Array Angular View

Figure 2.5: Porous Glass Emitter Array

After the manufacturing process, the same measurements were made to quantify emitter height, radius of curvature, and aspect ratio. The average height and radius of curvature are $247 \pm 2\mu m$ and $32 \pm 2\mu m$ respectively. Height maps of a ground emitter array measured using the optical profiler are shown in Figure 2.6. Measurement data for the three emitters manufactured and used in this test campaign are shown in Table 2.1.

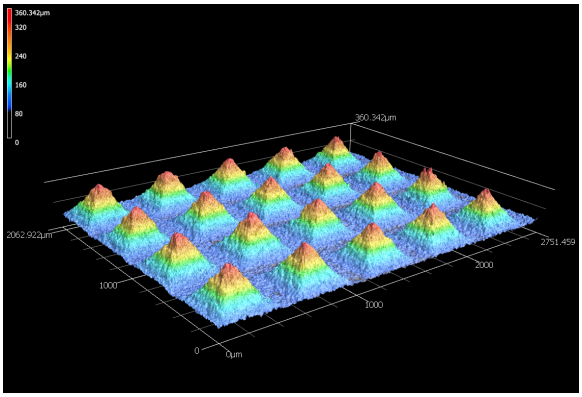

Figure 2.6: Height Map of Machined Emitter Array

The use of a grinding wheel to manufacture porous borosillicate glass emitter arrays has improved the overall geometry and uniformity of the emitter structures as compared to low speed CNC machining. This technique is more cost effective than upgrading current machinery to meet the spindle speed requirements proposed by Natisin et al. [13]. The main results obtained in this test campaign were collected through operating the porous glass thruster with the ground emitter arrays. These results are presented and discussed in a later section.

2.2 Extractor Alignment and Propellant Loading

While the thruster used here is similar to Natisin, a different propellant loading and extractor alignment procedure was used. The emitter-extractor grid alignment and propellant loading procedure described by Natisin et al. [13] is as follows: fully assemble the thruster, align the tips of the emitter structures with the center of the extractor grid holes under an optical microscope using the eight set screws around the perimeter of the extractor grid, use the four set screws at the base of the aluminum housing to raise the emitter array until the tips of the structures are in the same plane as the base of the extractor grid, remove the extractor grid, drip propellant directly onto the emitter array, place the extractor grid back onto the thruster, check the alignment and make any necessary adjustments.

With the thruster manufactured at the University of Illinois, it was found that in order to remove the extractor grid after alignment, the set screw positions needed to be altered. Once propellant was loaded directly onto the emitter array, the extractor grid would then have to be realigned with the emitter tips. When propellant saturates the porous emitter array, the borosilicate glass changes from white to transparent. The alignment procedure using an optical microscope is then unsatisfactory to achieve good emitter-extractor alignment. To ensure good alignment post propellant loading, the thruster was altered to allow for propellant loading from the rear, leaving the extractor grid fixed. A 0.25 inch hole was drilled in the base of the aluminum housing and PEEK emitter housing exposing the porous propellant reservoir as seen in Figure 2.7a.

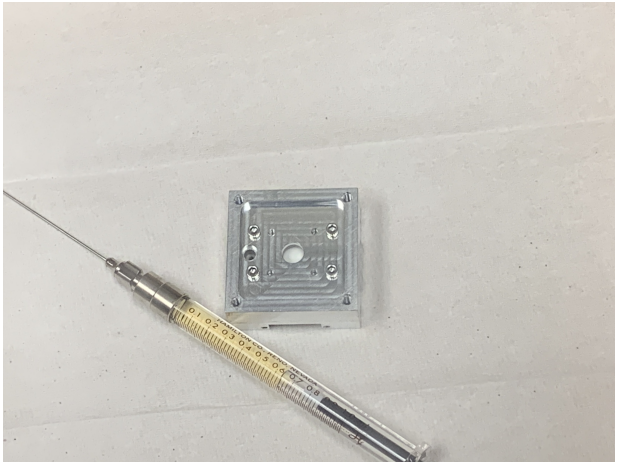

(a) Thruster positioned upside down for propellant loading

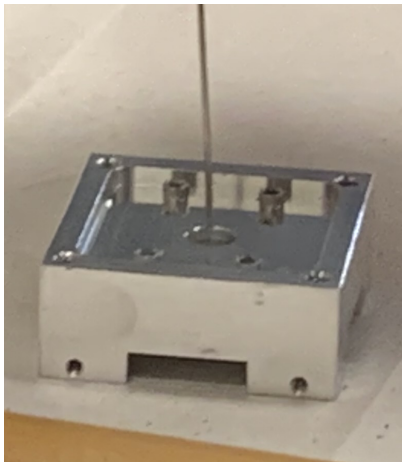

(b) Propellant loading via a luer lock syringe

Figure 2.7: Propellant Loading

For each experiement, the thruster was aligned before any propellant was loaded ensuring good alignment was achieved under an optical microscope. The four set screws located at the base of the aluminum housing were replaced with a 0.004 inch thick piece of aluminum shim stock to raise the emitter array decreasing the

emitter to extractor gap. Shim stock was used in place of the set screws as an attempt to keep the emitter to extractor gap fixed between multiple tests. The thruster was imaged using a 3D laser scanning confocal microscope to quantify the gap distance between the emitter and extractor before propellant loading. The measured emitter to extractor gap is reported for the specific thruster configured for each test. Figure 2.8 shows a 3D height map of the extractor grid and emitter tips used to measure the emitter to extractor gap distance.

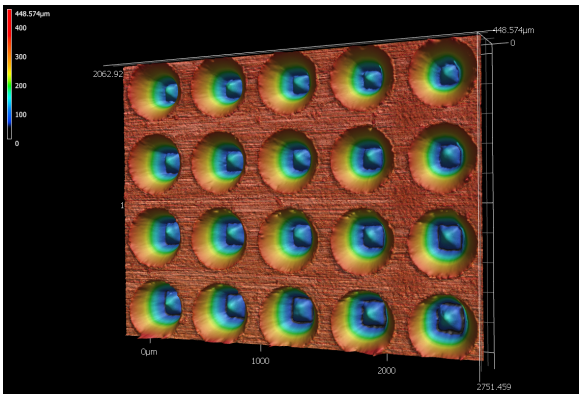

Figure 2.8: 3D height map of an assembled thruster

The distance between each emitter tip and the top plane of the extractor grid was measured. The thickness of the extractor grid was subtracted from the measurements and an average value of the emitter to extractor gap was then calculated. This process was repeated for each experiment. After alignment and gap quantification, the thruster was positioned extractor grid side down within a dry glovebox. Using a luer lock syringe, the desired amount of propellant was dripped directly onto the exposed porous reservoir and left to flow down through the reservoir and into the emitter array. The propellant loading process is shown in Figure 2.7. A multimeter was used to measure the resistance between the porous reservoir and the distal electrode. Prior to propellant loading, the resistance measurement was out of range of the multimeter ($> 60\text{M}\Omega$). It was found that when the emitter array was fully saturated, the resistance was less than 12 MΩ.

Table 2.1: Measured Emitter Geometry Parameters

Emitter Name	Manufacturing Process	Radius of Curvature	Height	Aspect Ratio
PE-1	Low Speed CNC	63 μm	172 μm	–
PE-2	Grinding Wheel	31.2 μm	243.65 μm	0.68
PE-3	Grinding Wheel	29.5 μm	249.37 μm	0.68
PE-4	Grinding Wheel	33.9 μm	247.39 μm	0.65
PE-5	Laser Ablation	50 μm	210 μm	0.82
Natisin et al.	High Speed CNC	$10 - 20$ μm	300 μm	–

Chapter 3

Experimental Setup

This test campaign was carried out in a vacuum chamber pumped using a turbo pump backed by a mechanical rough pump. Chamber pressure was approximately 10^{-6} Torr at the beginning of thruster operation. The thruster was passively fed propellant for all tests; the propellant was loaded directly onto the porous glass reservoir and emitter array, so an external feed system was not needed. The diagnostics used for plume characterization consisted of a 316 stainless steel target plate, a retarding potential analyzer, and a linear time of flight spectrometer. The thruster was positioned on a vacuum compatible rotary stage allowing for rapid transition from one diagnostic technique to another. Figure 3.1 shows an image of the thruster positioned inside of the chamber aligned along the centerline of the collector plate, as well as rotated towards a retarding potential analyzer (RPA) and time of flight mass spectrometer (ToF-MS) instrument. A diagram of the ToF-MS/RPA is shown in Figure 3.2.

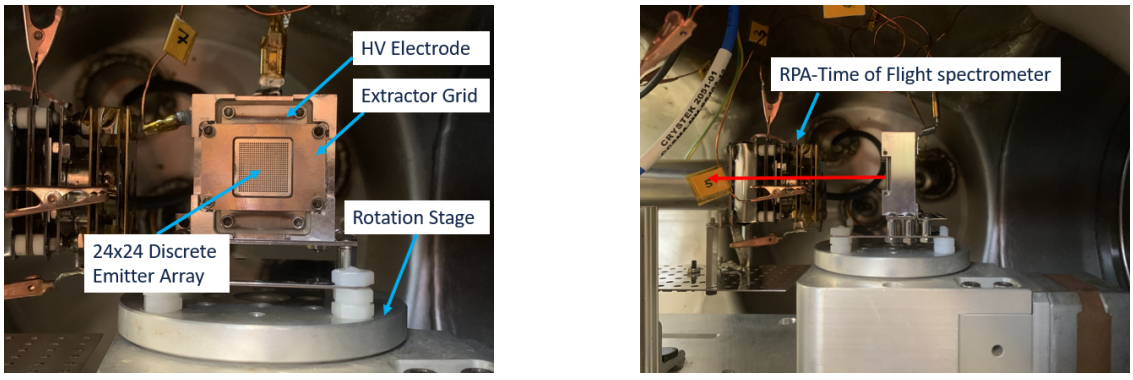

(a) **(b)**

Figure 3.1: Image of (a) the assembled thruster mounted within the vacuum chamber, and (b) the thruster rotated toward the RPA-ToF instrument. The red arrow in (b) represents the direction of the plume.

3.1 Emitter, Extractor, and Target Current Measurements

A 316 stainless steel collector plate was used to intercept the thruster plume and measure the current as a function of the applied emitter voltage during operation. The plate was built to intercept the plume up to 45° off centerline. Measurements were made with the same instrumentation set up used by Lyne et al. [3] to characterize FAM-110A electrospray operation in a capillary style thruster. Emitter current and voltage was measured through a Matsusada AMS-5B6-L1 high voltage amplifier, and interfaced with a National Instruments data acquisition (DAQ) module (NI USB-6210). Extractor current was measured using a standard transimpedance amplifier configuration and recorded using the DAQ. Collector current was measured using a picoammeter (Keithley Model 6485) and recorded by the DAQ.

The thruster was operated in a triangle wave configuration with a peak to peak value twice that of the maximum applied emitter bias, and a frequency of 0.2 Hz. Multiple waveforms were collected during each experiment to gain a thorough understanding of the behavior of thruster currents as a function of the applied emitter bias. The current data was separated into bins and average current and voltage quantities were calculated for each bin. All of the waveforms for a given experiment were then averaged together to obtain comprehensive IV curves for the propellants being tested.

3.2 Retarding Potential Analyzer

A retarding potential analyzer (RPA) is commonly used to measure the electric potential distribution of charged particles in an electrospray plume. An RPA measures the collected current of the plume as a series of grids, upstream from the collector, are swept between a minimum and a maximum retarding potential. When the retarding potential reaches the same energy as species within the plume, the particles at that energy are rejected and the collected current measurement changes. When the retarding potential exceeds that of the full beam potential, all charged particles are rejected by the grids and the measured current reaches a minimum. Knowing the electric potential distribution of the plume is essential to further measurements such as time of flight spectrometer, as well as predicting performance of an electrospray thruster.

An RPA was used in this test campaign to measure the kinetic energy distribution of the thruster plume as described above. In the experiments carried out in this work, the RPA grids were integrated onto the time of flight mass spectrometer as shown in Figure 3.2. A high voltage amplifier was used to bias the RPA grids with a triangular waveform ramped between 0 V and a maximum retarding potential. The maximum retarding potential must exceed the beam potential in order to reach full saturation of the signal, and thus was determined based on the operating conditions of the thruster during each experiment. A collector downstream

of the thruster plume monitored current while the RPA bias was swept. The collected current was averaged over multiple periods by a digital oscilloscope. RPA measurements were taken for both positive and negative emission polarity.

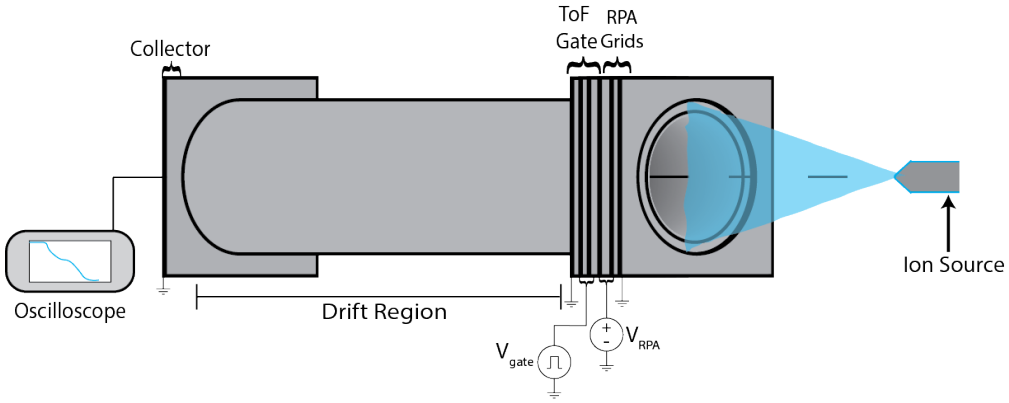

Figure 3.2: Diagram of the Time of Flight Mass Spectrometer and Retarding Potential Analyzer

3.3 Time of Flight Mass Spectrometer

Time of flight mass spectrometry (ToF-MS) is a useful tool for electrospray plume characterization and performance quantification. ToF-MS is used to compute the mass to charge ratio distributions within a plume giving insight into the species present. ToF-MS measures the time taken for a charged particle to traverse a known distance in a region free of external fields, thus allowing the particle's velocity to be calculated. If the velocity is gained by acceleration through a known potential, then the mass to charge ratio can be computed from equation 3.1 [14].

$$\frac{m}{q} = 2V_B \left(\frac{t}{L}\right)^2 \tag{3.1}$$

Where V_B is the beam potential, t is the flight time of the particle, and L is the length of the field free region. In a linear ToF-MS, an electrostatic gate is used to either block the incoming electrospray plume (gate closed) or allow the plume to enter the flight tube (gate open). The triggering of the gate is set to time $t = 0$ for mass to charge ratio computations.

The instrument used to measure retarding potential and time of flight mass spectrometry data was the same instrument proposed by Lyne et al. [15]. This instrument is a linear ToF-MS which is much simpler design than the orthogonal ToF-MS used in [16]. In this work, the ToF-MS data was acquired by a digital oscilloscope. Multiple time-of-flight signals were captured in a single waveform acquisition. The waveform was

then split into segments, each of which correspond to a single ToF signal. These signals were then averaged together to improve the signal to noise ratio. Lyne demonstrated that the quality of time-of-flight signals measured increases with the number of averages taken [15], and discusses the design and operation of this particular ToF-MS in greater detail.

Chapter 4

Results and Discussion

This section describes the results obtained using the experimental setup overviewed above. The thruster was operated with 1-Ethyl-3-methylimidazolium tetrafluoroborate (EMIM-BF_4), a widely used electrospray propellant, and FAM-110A for comparison of the measured plume characteristics, as well as a comparison of predicted thruster performance metrics. The section is presented in the following order: current as a function of applied emitter voltage, RPA results, ToF-MS results, and predicted performance calculations. Comparisons are made between the two different propellants as well as existing literature data. Different porous emitter arrays were used in each experiment. The geometry of each emitter was characterized and those results are found in Table 2.1.

4.1 Current and Voltage Measurements

4.1.1 Preliminary Measurements with CNC Milled Emitter Arrays

The porous glass electrospray thruster was operated with both EMIM-BF_4 and FAM-110A using the low speed CNC machined emitter arrays. Propellant was loaded from the rear hole machined into the thruster body as described previously. Shim stock was not yet used to adjust the emitter to extractor gap distance. The four set screws located at the base of the thruster housing were used to adjust this distance. Emitter PE-1 was used in operation with both propellants. Between experiments, the emitter array was soaked in deionized water to flush out any traces of propellant. Emitter geometry measurements are found in Table 2.1. The emitter to extractor gap distance was 128 μm and 180 μm for the EMIM-BF_4 and FAM-110A experiments respectively.

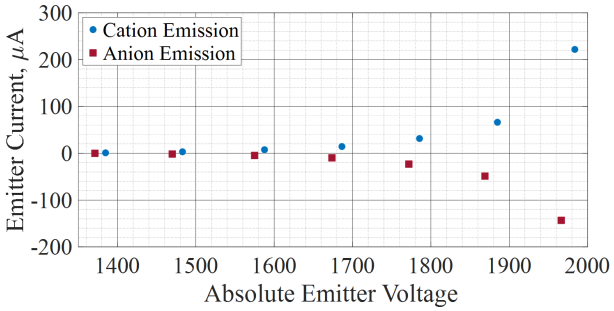

Figure 4.1: EMIM-BF_4 emitter current v.s. applied emitter bias

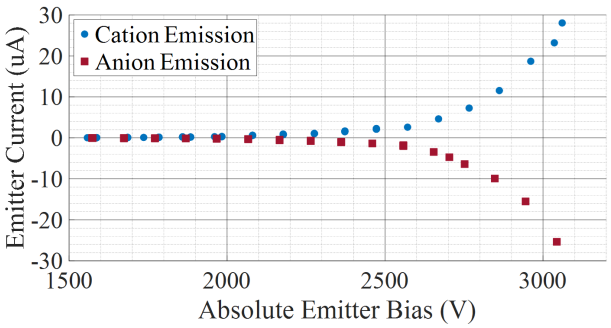

Figure 4.2: FAM-110A emitter current v.s. applied emitter bias

The emitter current as a function of the applied emitter voltage is shown in Figures 4.1 and 4.2 for EMIM-BF_4 and FAM-110A respectively. The thruster operated in a bi-polar configuration. The emitter was biased with a square wave at a polarity switching frequency of 0.5 Hz. Despite the poor geometry of the CNC machined emitter arrays, the thruster was able to operate with both propellants. The onset voltage during EMIM-BF_4 operation was approximately 1483 V. Emitter currents of approximately 222 μA and -144 μm were measured at emitter voltages of 1984 V and -1966 V respectively. The onset voltage during FAM-110A operation was approximately 2000 V. Emitter currents of approximately 28 μA and -25 μA were measured at emitter voltages of 3060 V and -3043 V respectively. The large difference in onset voltage can be attributed to the difference in the emitter to extractor gap distance. During operation with FAM-110A a larger voltage was needed to produce the required electric field strength for charged particle emission. As a consequence of the higher gap distance i.e. the larger onset voltage, much higher voltages were needed to operate the FAM-110A propellant, and the magnitude of emitter current measured during EMIM-BF_4 operation was not attainable.

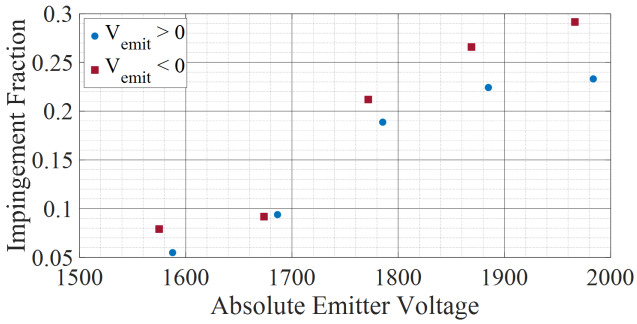

Figure 4.3: EMIM-BF_4 extractor impingement fraction

The extractor impingement fraction as a function of the applied emitter bias for EMIM-BF_4 is shown in Figure 4.3. The thruster showed a higher impingement fraction with anion emission, reaching a maximum of approximately 29%. The maximum impingement fraction during cation emission was approximately 23%.

In both polarities, the impingement fraction increased as a function of the emitter voltage. One possible explanation is the widening of the Taylor cone emission sites as the emitter voltage increases. The wider the emission site, the more current will impinge upon the extractor grid.

The preliminary measurement data presented here serves to show that thruster operation was still possible using low speed CNC machined emitter arrays with both of the propellants of interest. It also serves as the motivation for the improvements made to the UIUC thruster described previously. The remaining results presented in this section were acquired through thruster operation using the grinding wheel fabricated emitter arrays. Main conclusions and comparisons between the propellants of interest are drawn using the data in the remainder of this work.

4.1.2 Current and Voltage Measurements with Grinding Wheel Fabricated Emitters

The porous glass electrospray thruster was first operated with EMIM-BF_4 using the grinding wheel fabricated emitter arrays. Thruster propellant loading and alignment was done according to the procedures described previously. For all current and voltage measurements, the thruster was operated in a bi-polar configuration. The emitter bias was a symmetric triangular waveform operated at 0.2 Hz. Two experiments were conducted with EMIM-BF_4 and compared with the data presented in [13]. The two EMIM-BF_4 experiments correspond to the emitter geometry of PE-2 and PE-3 in Table 2.1. The mean emitter to extractor gap distance was 76 μm and 68 μm for the thruster using PE-2 and PE-3 respectively.

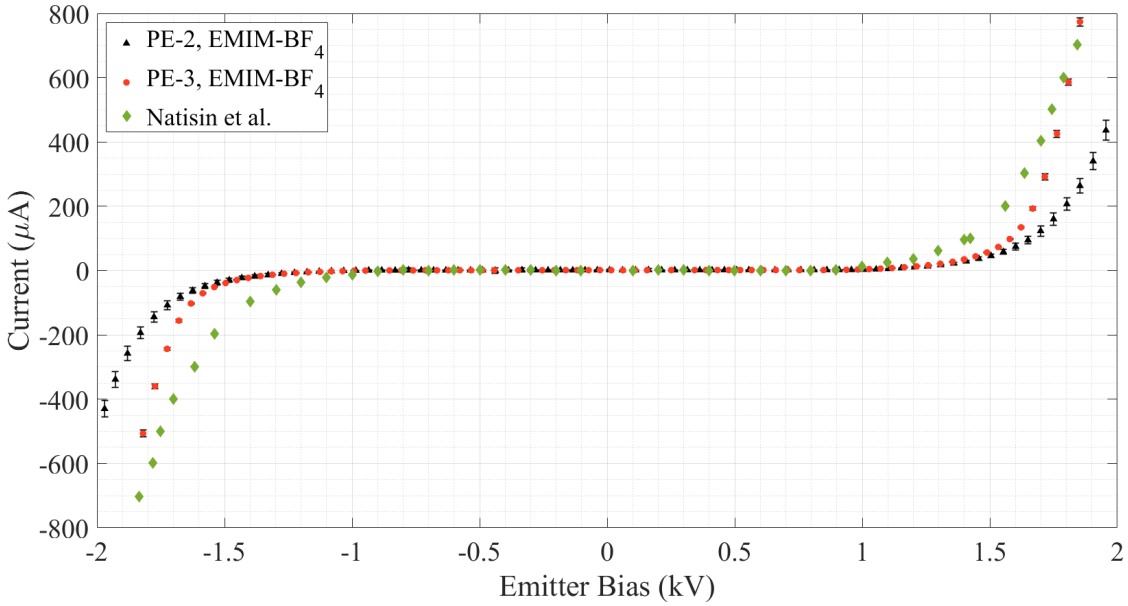

Figure 4.4: Emitter current v.s. emitter bias for the two EMIM-BF_4 experiments

The measured emitter current plotted as a function of the applied emitter bias is shown in Figure 4.4. Measured emitter current data from [13] is included for comparison. Using PE-2, emitter currents of approximately 436 μA and 430 μA were achieved at voltages of +1955 V and -1970 V respectively. Initial signs of charged particle emission was observed at $\pm 957V$ in both positive and negative polarity. Using PE-3, emitter currents of approximately 770 μA and 507 μA were achieved at voltages of +1850 V and -1820 V respectively. Initial signs of emission were observed at $\pm 893V$ for both positive and negative emission polarity. Differences in onset voltage current emission between the two EMIM-BF_4 experiments can be attributed to small differences in the radius of curvature of the emitters used, as well as the emitter to extractor gap distance. Both of these parameters effect the electric field strength between the emitter and extractor grid. A smaller radius of curvature (sharper tip) and emitter to extractor gap increase the electric field strength. In both experiments, more emission current was observed during cation emission at each emitter voltage. This is consistent with the current emission data presented in [13].

Comparing emitter current using PE-3 to the emitter current in [13], the UIUC thruster attained similar results with a grinding wheel fabricated emitter array. Natisin et al. reported emission currents up to $\pm 700\,\mu A$ at emitter voltages of +1845 and -1835 V for positive and negative emission polarity. The onset voltages reported were approximately $\pm 800\,V$. The radius of curvature of the emitters reported by Natisin et al. was between $10 - 20\,\mu m$. The emitter to extractor gap distance was measured to be 0 μm i.e. the emitter tips were even with the bottom plane of the extractor grid.

The current intercepted by the extractor grid is plotted as a function of the emitter bias in Figures 4.5 and 4.6. Extractor current is expressed in terms of the measured current value and as a fraction of the total measured emitter current.

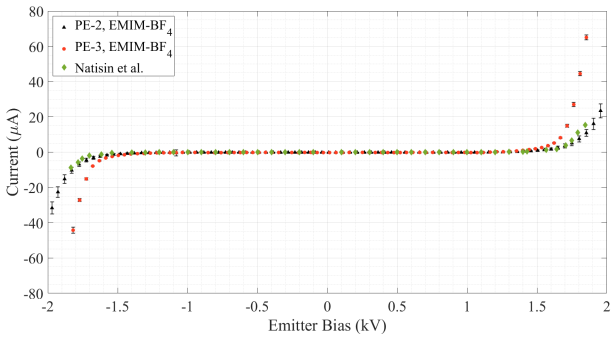

Figure 4.5: EMIM-BF_4 extractor current v.s. applied emitter bias

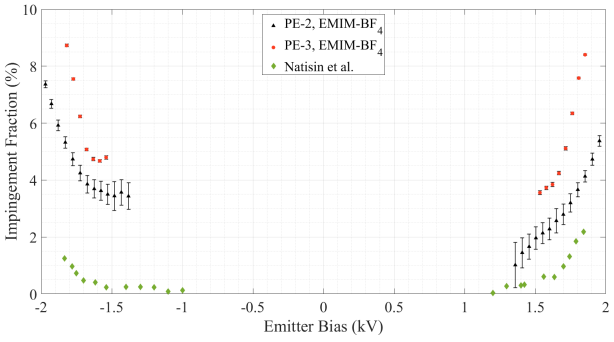

Figure 4.6: EMIM-BF_4 current impingement fraction v.s. applied emitter bias

Extractor impingement current remained below 9% during thruster operation with both emitter arrays. In both experiments, more extractor current was measured during anion emission. Less extractor impingement

current was observed during thruster operating with PE-2. A maximum of 7.4% and 5.4% of the emitter current impinged on the extractor grid during anion and cation emission respectively. As the emitter voltage is increased, the current impingement on the extractor increases. This is due to increased plume divergence at higher voltages. The disparity between the impingement fractions during each experiment is most likely due to differences in extractor grid alignment. The thruster operating with PE-3 had a smaller emitter mean radius of curvature, and a smaller emitter to extractor gap. As stated previously, the extractor grid is aligned each time the thruster is assembled via 2-56 set screws. Variation in extractor grid alignment will change the amount of emitter current intercepted by the grid. The impingement fraction reported in [13] remained below 1% at emission currents up to 500 μA in positive mode and currents up to $-700\,\mu A$ in negative mode. The increased extractor impingement current in the UIUC thruster is due to the larger emitter to extractor gap and possibly difference in alignment between the thruster presented in this work and that in [13].

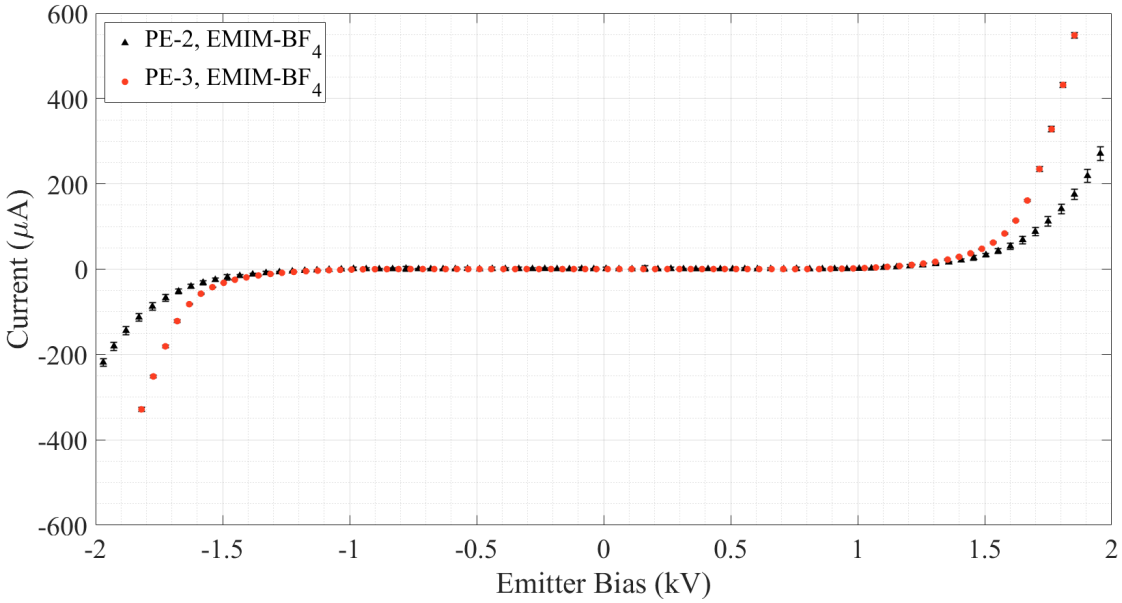

Figure 4.7: Collector current v.s. emitter bias for the two EMIM-BF_4 experiments

Current measured by a collector plate downstream of the thruster is plotted as a function of the emitter bias in Figure 4.7. Under ideal conditions, the sum of the extractor and collector current should be equal to the total emitter current at each voltage. After thruster operation, discoloration on the mounting plate for the thruster, shown in Figure 4.8, was observed. This is evidence of plume impingement on the thruster mounting plate. Discoloration could also be due to sputtered material and/or secondary species emission from the various surfaces within the vacuum chamber. This impingement means some of the plume was lost during collector plate measurements accounting for the discrepancy of the sum of the extractor and collector

current.

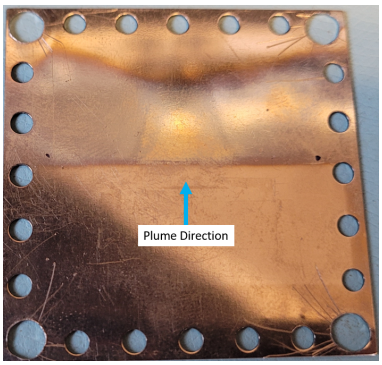

Figure 4.8: Thruster mounting plate after operation with EMIM-BF_4

Overall, the grinding wheel fabricated emitters have significantly increased emission current, decreased extractor impingement current, and decreased the onset voltage of the UIUC thruster as compared to operation with low speed CNC machined emitter arrays. The results presented above have proven comparable to the current emission data presented in [13]. Next, the thruser was operated using the FAM-110A multimode propellant and data were compared to the EMIM-BF_4 current emission data using PE-3 (best results case). The PE-4 emitter array was used during thruster operation with FAM-110A. Geometry parameters for PE-4 are shown in Table 2.1. The mean emitter to extractor gap distance was approximately 82 μm. Emitter current is plotted as a function of the applied emitter bias in Figure 4.9 for both EMIM-BF_4 and FAM-110A.

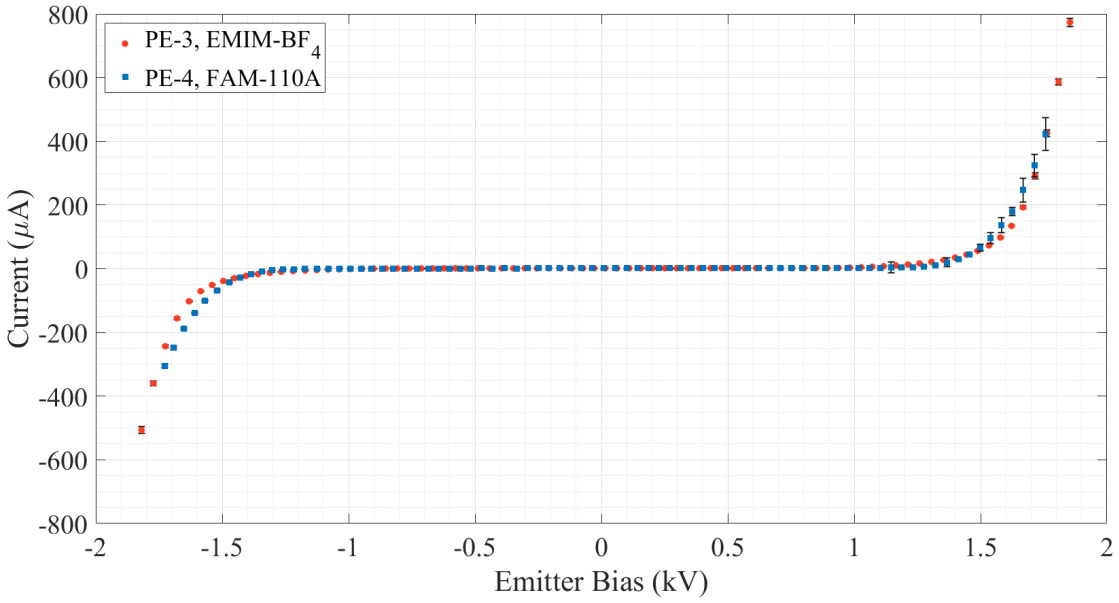

Figure 4.9: Emitter current v.s. emitter bias for FAM-110A and EMIM-BF_4

During operation with FAM-110A, emitter currents of 422 μA and 305 μA were observed at voltages of

+1760 V and -1730 V respectively. First signs of emission were observed at $\pm 883\,V$ for anion and cation emission. Comparatively, during operation with EMIM-BF_4, emitter currents of 425 μA and 243 μA were observed at voltages of +1760 V and -1730 V respectively. For both cation and anion emission, between emitter voltages of 1500 V and 1720 V, FAM-110A emitted more current at each voltage than EMIM-BF_4. Comparing emitter geometries between the two experiments, the thruster using PE-4 had 4.4 μm larger radius of curvature and a 14 μm larger emitter to extractor gap distance. Despite this, FAM-110A demonstrated higher current emission and lower onset voltage than EMIM-BF_4. For comparable emission current, the FAM-110A propellant has a lower power requirement. This is shown in Figure 4.10.

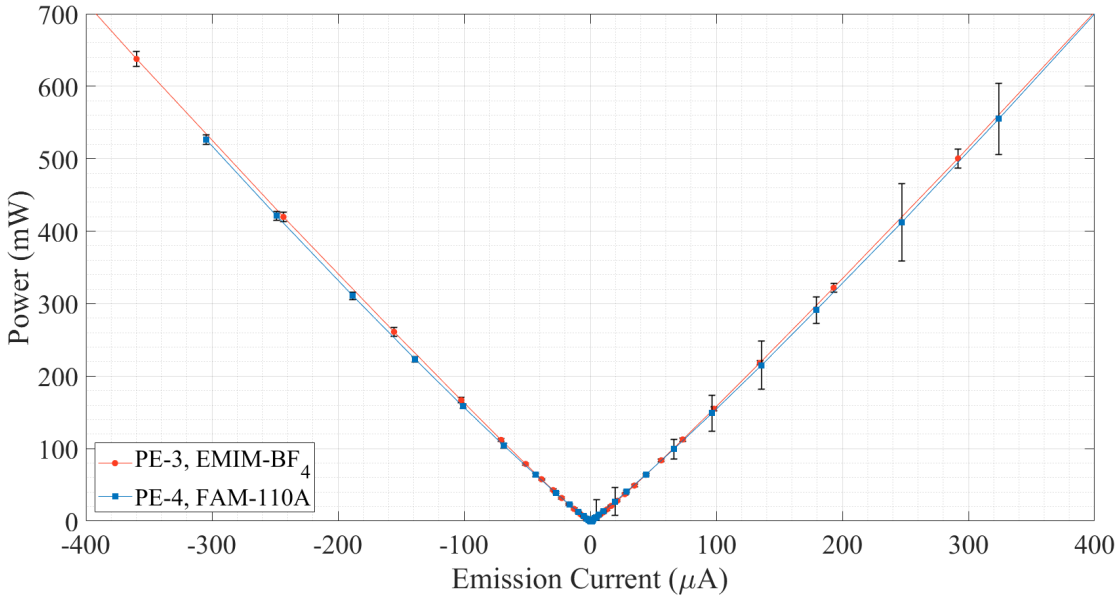

Figure 4.10: Thruster power v.s. emission current for FAM-110A and EMIM-BF_4

Ma et al. performed similar current measurements operating their PET-100 porous glass electrospray thruster with FAM-110A [17]. Similar trends in emission current were reported. Onset voltages of $\pm 1500\,V$ and $\pm 2000\,V$ were observed for FAM-110A and EMIM-BF_4. The thruster operating with FAM-110A emitted more current at comparable voltages much like what is being observed in this work. The measured extractor current as a function of the applied emitter voltages is shown in Figures 4.11 and 4.12.

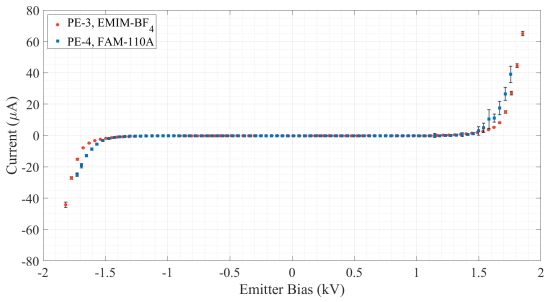

Figure 4.11: FAM110-A and EMIM-BF_4 extractor current v.s. applied emitter bias

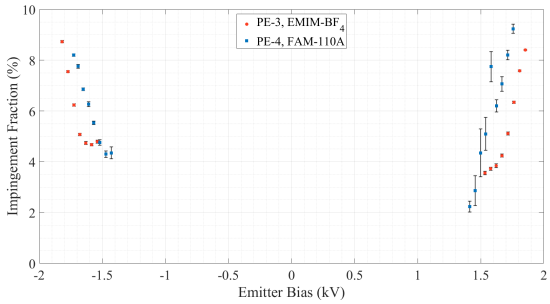

Figure 4.12: FAM-110A and EMIM-BF_4 current impingement fraction v.s. applied emitter bias

FAM-110A showed similar extractor impingement current trends to EMIM-BF_4. Impingment fraction stayed below 8.5% in anion emission and reached upwards of 9.25% in cation emission. The current intercepted by the extractor grid increased as a function of the applied emitter bias due to increased beam divergence. In anion emission, FAM-110A had 0.5% less intercepted current than EMIM-BF_4. In cation emission mode, FAM-110A had approximately 0.6% more intercepted current. The emitter to extractor gap distance was 14 μm larger during thruster operation with FAM-110A, this could lead to higher extractor impingement fractions when compared to the thruster operation with EMIM-BF_4.

Current measured by a collector plate downstream of the thruster as a function of the applied emitter voltage is shown in Figure 4.13.

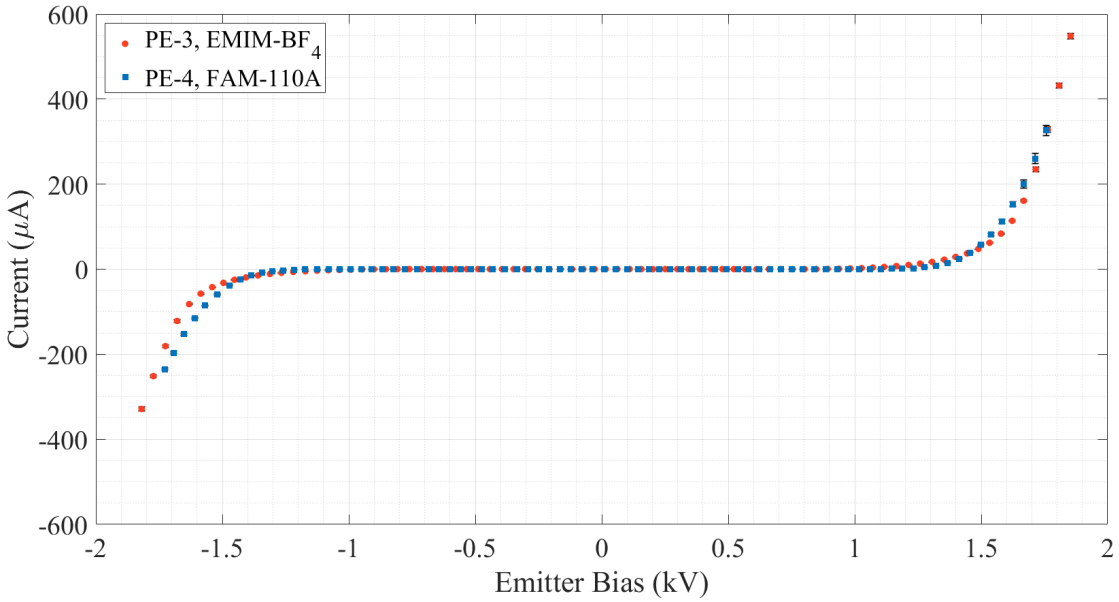

Figure 4.13: Collector current v.s. emission current for FAM-110A and EMIM-BF_4

Currents of 326 μA and 235 μA were measured at +1760 V and -1730 V respectively. Consitant with the

emitter current results, more current was measured at comparative voltages during thruster operating with FAM-110A.

4.2 Retarding Potential Analyzer Results

A retarding potential analyzer was used to measure the kinetic energy distribution of the electropspray plume operating with EMIM-BF_4 and FAM-110A. The data presented in this section for EMIM-BF_4 correspond to the thruster operating with emitter PE-3. For both propellants, the thruster operated in a bi-polar configuration. The emitter bias was a square wave with a polarity switching frequency of 5 seconds. The emitter bias was synced with the RPA so during data collection, the thruster would hold either a positive or negative polarity. RPA data was taken at an emitter bias of $\pm 1500\,V$, $\pm 1600\,V$, and $\pm 1700\,V$. The cumulative energy spectrum for EMIM-BF_4 at $V_{emit} = \pm 1500\,V$ is shown in Figure 4.14.

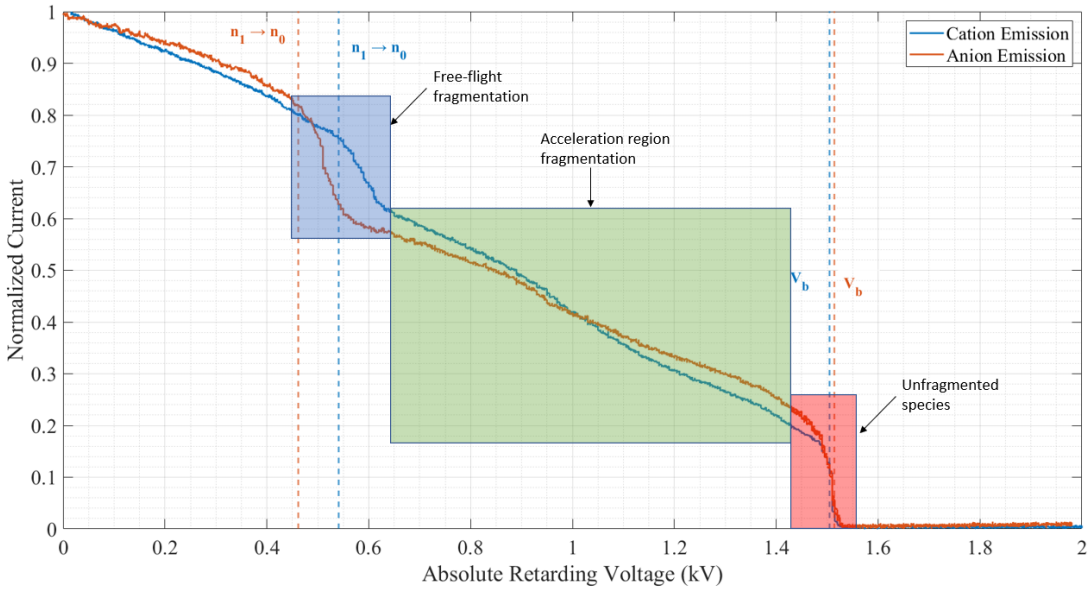

Figure 4.14: Cumulative energy spectrum for EMIM-BF_4, $V_{emit} = \pm 1500\,V$

Multiple features are seen in the cumulative energy spectrum due to species fragmentation during and after charged particle emission. Species that fragment after passing through the extractor grid apertures (in free flight), will maintain the same velocity with a lower mass, thus at a different kinetic energy. These species will be blocked at a lower potential by the retarding grid than other non-fragmented species in the plume. The retarding potential of different fragmentation processes can be calculated using equation 4.1. Species that fragment within the acceleration region of the thruster (between the emitter and extractor grid) experience a change in mass, but are further accelerated. The amount of acceleration experienced depends

upon the location of fragmentation within the acceleration region. This mechanism appears as a continuous range of kinetic energies between the free-flight fragmentation region and the unfragmented species [13]

The vertical dashed lines displayed in Figure 4.14 represent energies of the dimer to monomer fragmentation process calculated using equation 4.1.

$$V_{i \to j} = V_b \frac{m_j}{m_i} \tag{4.1}$$

Where V_b is the energy of the unfragmented species, subscript i indicates the original species, and subscript j indicates the fragmented species. In Figure 4.14, the first prominent feature in both emission polarities is the large step in current near the predicted energy for $n_1 \to n_0$ fragmentation. The different species are denoted by lower case n with the subscript corresponding to the amount of neutral pairs ($n_0 = monomer$, $n_1 = dimer$, $n_2 = trimer$). Between a retarding potential of approximately 600 V and 1400 V, the measured current follows a steady decreasing trend indicative of acceleration region fragmentation. The large step in current between 1400 V and 1600 V is the unfragmented species being retarded at the unfragmented beam voltage (V_b). The unfragmented species appear at a lower voltage than the applied emitter voltage due to energy losses in the electropsray process. The measured beam voltage as well as the energy efficiency ($\eta_\epsilon = V_b/V_{emit}$) at each emitter voltage is shown in Table 4.1. The region between 0 V and 400 V shows a steady decreasing current as the retarding voltage is increased. This is most likely due to off axis ions lost while traveling towards the collector. As stated previously, the retarding potential grids have been integrated at the entrance of the ToF-MS. The particles with enough energy to pass through the grids must travel 120 mm through the flight tube before being detected by the collector. As the plume travels this distance, charged particles could be lost to the walls of the flight tube decreasing the measured current as the retarding voltage is increased.

Table 4.1: EMIM-BF_4 beam voltage and energy efficiency

V_{emit} (V)	V_b (V)	η_ϵ
-1700	-1665	97.9%
-1600	-1590	99.4%
-1500	-1480	98.7%
1500	1490	99.3%
1600	1580	98.75%
1700	1640	96.5%

The RPA data shown here is consistent with other EMIM-BF_4 RPA data in literature. The cumulative energy spectrum presented by Natisin et al. clearly shows $n_1 \to n_0$ fragmentation in both polarities [13], as well as the acceleration region fragmentation. Further comparing with the RPA data taken by Ma [10]

and Klosterman [18], the data taken at UIUC shows similar cumulative energy spectrum for EMIM-BF_4. Figures 4.15 and 4.16 show the cumulative energy spectrum for FAM-110A for positive and negative polarity respectively.

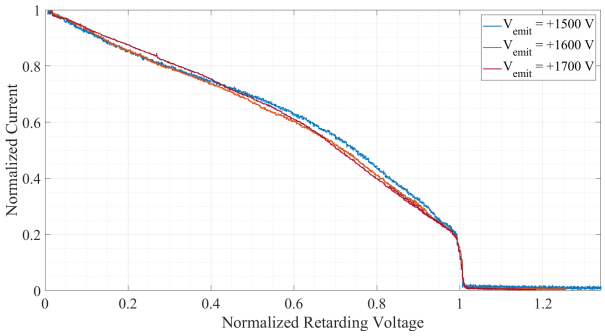

Figure 4.15: FAM110-A cation emission cumulative energy spectrum. RPA bias is normalized by the emitter bias.

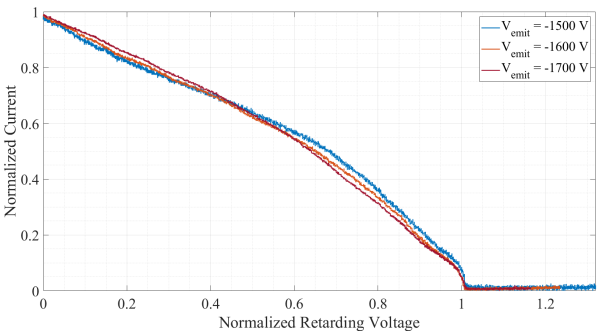

Figure 4.16: FAM110-A anion emission cumulative energy spectrum. RPA bias is normalized by the emitter bias.

Three different regions are observed in the energy spectrum for FAM-110A. First, an initial linear decline between 0 and approximately 60% of the emitter voltage in both cation and anion emission. This region, similar to what is shown in the EMIM-BF_4 spectrum, could be due to off axis ions being lost in the plume as it travels through the flight tube. A second linear decline region with a different slope is observed between 60% and approximately 97% of V_{emit} in both polarities. This region is most likely represents the species fragmented within the acceleration region of the thruster. The most prominent feature in both polarities is the large step in current appearing near the emitter voltage. This represents the energy of the unfragmented species in the plume. These data align well with Ma et al. [17], who took RPA measurements of FAM-110A operating the PET-100 thruster. In both results, no large steps in the current indicating field free fragmentation occur as seen in the data for EMIM-BF_4. The measured beam voltage and energy efficiency at each polarity for FAM-110A is shown in Table 4.2.

Table 4.2: FAM-110A beam voltage and energy efficiency

V_{emit} (V)	V_b (V)	η_ϵ
-1700	-1680	98.8%
-1600	-1581	98.8%
-1500	-1494	99.6%
1500	1496	99.7%
1600	1590	99.4%
1700	1690	99.4%

The FAM-110A propellant appears to be more mono-energetic than that of EMIM-BF_4. The unfragmented species retain more energy in FAM-110A. The average energy efficiency across all polarities for FAM-110A is

99.3% as compared to 98.4% for EMIM-BF_4.

4.3 Time of Flight Mass Sepctrometry Results

A time of flight mass spectrometer was used to analyze the species present in the electrospray plumes of EMIM-BF_4 and FAM-110A. The data presented for EMIM-BF_4 correspond to the thruster operating with emitter PE-3. For both propellants, the thruster operated in a bi-polar configuration. The emitter bias was a square wave with a 5 second polarity switching frequency. The thruster would hold the polarity while ToF-MS measurements were being recorded. Measurements were made at emitter voltages of $\pm 1500\,V$, $\pm 1600\,V$, and $\pm 1700\,V$. The cumulative spectrum for EMIM-BF_4 at $\pm 1500\,V$ is shown in Figure 4.17.

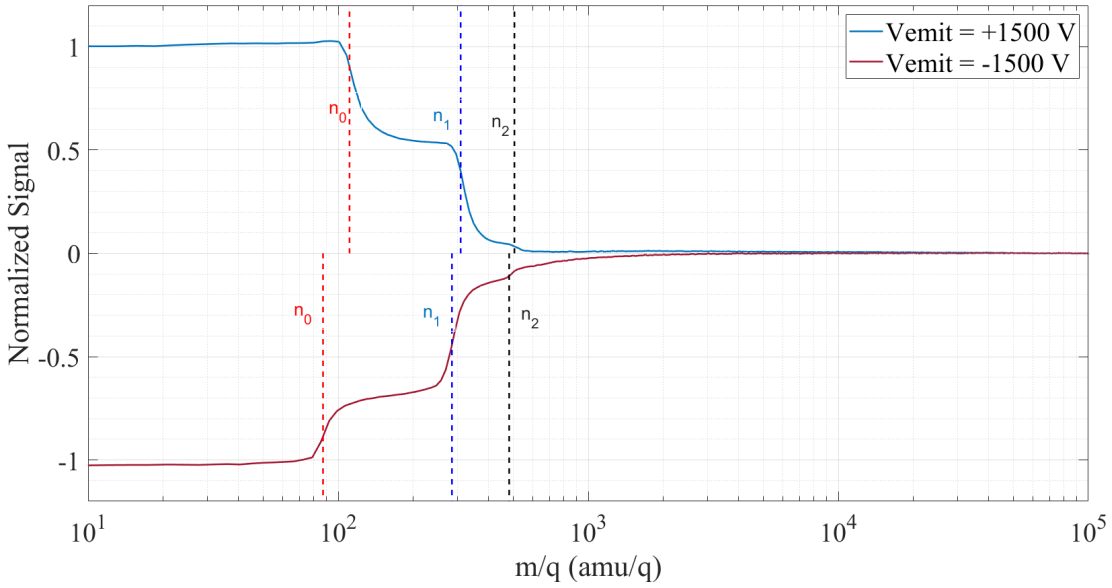

Figure 4.17: Cumulative mass to charge spectrum for EMIM-BF_4

The masses of the expected species emitted in the plume are plotted as vertical dashed lines. For EMIM-BF_4 the expected species take the form of the cation [EMIM+] during positive polarity and the anion [BF_4-] during negative polarity plus additional neutral pairs. The subscript denotes the number of neutral pairs. The data shows distinct steps in the measured current near the mass values expected for the monomer (n_0) and dimer (n_1) species in both polarities. A smaller current step is observed near the mass value for the trimer (n_2) species in both polarities. In cation emission, the plume is comprised of approximately 46% monomers, 48% dimers, and 3% trimers. In anion emission, the plume is comprised of approximately 32% monomers, 51% dimers, and 5% trimers. The remaining percentage of the signal could be comprised of other species such as tetramers that could not be resolved by this instrument.

The data for EMIM-BF_4 align very closely with that presented in [13]. Natisin et al. measured a signal comprising of 45% monomers, 47% dimers, and 6% trimers in cation emission. During anion emission, the measured current showed a plume comprising of 39% monomers, 51% dimers, and 8% trimers. Overall it is clear that the plume of EMIM-BF_4 is made up of dominantly dimers and monomers with a small fraction of the plume being trimers in both emission polarities. Arguments can be made that species such as tetramers are also present in the plume.

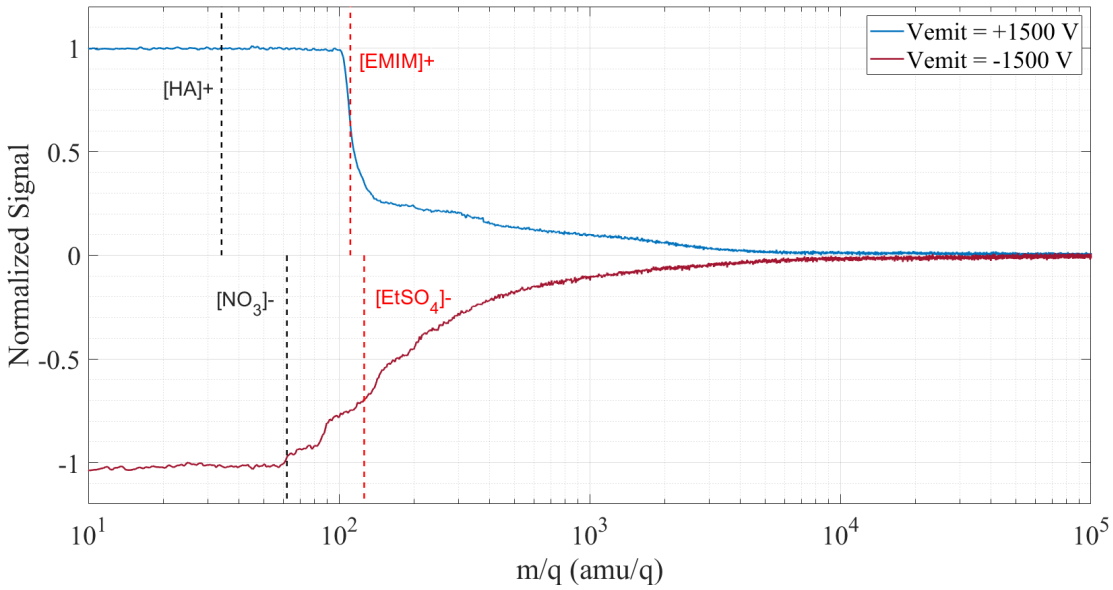

Figure 4.18: Cumulative mass to charge spectrum for FAM-110A

The cumulative mass to charge spectrum for FAM-110A is shown in Figure 4.18. The verticle dashed lines represent the mass to charge ratios of the know monomers in the propellant. The know cations are hydroxylamine ([HA+]) and [EMIM+]. The know anions are nitrate ([NO_3-]), and ethylsulfate ([$EtSO_4$-]). The mass to charge ratios of the known monomer species, as well as predicted dimer and timer species are found in Table 4.3. In cation emission mode, the most prominent step in the signal occurs near the expected mass of [EMIM+]. There are no observable features at lower mass to charge ratios indicating that the hydroxylamine cation ($m/q = 34amu/q$) is not present in the plume. Wainwright et al. conducted quadropole mass spectrometry on FAM-110A propellant and arrived at a similar conclusion [8]. There were no spectra peaks found that represent the hydroxylamine cation. Zhou et al. examined ESI mass speectra of pure HAN solutions [19]. They found that no intact HAN species were detected in the positive electrospray mode. It was revealed that the dissociative reaction of $HONH_2 \cdot HNO_3$ with H^+ rationalizes the lack of intact HAN species in a positive electrospray plume. It can be argued that another, much smaller step in signal occurs near 354 amu/q, corresponding to the [HA+][HA-$EtSO_4$]$_2$ trimer. Overall, the positive plume composition

is dominated by the [EMIM+] monomer. Less species were observed during positive mode operation with FAM-110A as compared to EMIM-BF_4.

In anion emission, multiple species are observed in the electrospray plume. Of the known anions in the propellant, steps in the signal can be observed near the expected masses of both nitrate and ethylsulfate. Another species is observed between these two masses at approximately 85 amu/q. Looking at higher masses than the $EtSO_4$ anion, two possible species can be observed. One at approximately 145 amu/q and another at approximately 200 amu/q. Peaks in mass spectra near 80, 148, and 196 were observed by Wainwright in anion emission mode [8], near what is being observed in the data presented in this work.

Table 4.3: Predicted species within FAM-110A plume

Positive emission		Negative emission	
Species	m/q (amu/q)	Species	m/q (amu/q)
EMIM	111	NO_3	62
HA	34	$EtSO_4$	126
$[EMIM][EMIM \cdot NO_3]$	284	$[NO_3][NO_3 \cdot EMIM]$	235
$[EMIM][EMIM \cdot EtSO_4]$	348	$[NO_3][NO_3 \cdot HA]$	158
$[HA][HA \cdot NO_3]$	130	$[EtSO_4][EtSO_4 \cdot EMIM]$	363
$[HA][HA \cdot EtSO_4]$	194	$[EtSO_4][EtSO_4 \cdot HA]$	286
$[EMIM][EMIM \cdot NO_3]_2$	457	$[NO_3][NO_3 \cdot EMIM]_2$	408
$[EMIM][EMIM \cdot EtSO_4]_2$	585	$[NO_3][NO_3 \cdot HA]_2$	254
$[HA][HA \cdot NO_3]_2$	226	$[EtSO_4][EtSO_4 \cdot EMIM]_2$	600
$[HA][HA \cdot EtSO_4]_2$	354	$[EtSO_4][EtSO_4 \cdot HA]_2$	446

4.4 Predicted Thruster Performance

Using the information on species mass and the relative intensities of the time of flight signal data, the specific impulse can be estimated using equation 4.2.

$$I_{sp} = \frac{T}{\dot{m} g_0} \tag{4.2}$$

Where T is the thrust, $\dot{m}$ is the mass flow rate, and g_0 is the standard acceleration due to gravity on earth. Thrust and mass flow rate can be calculated from the measured time of flight data according to [11].

$$T_{ToF} = -\frac{2|V_e|}{L^2} \int_0^\infty t \frac{dI}{dt}\, dt \tag{4.3}$$

$$\dot{m}_{ToF} = -\frac{2V_e}{L^2}\int_0^\infty t^2 \frac{dI}{dt}\, dt \tag{4.4}$$

Where V_e is the emitter voltage, L is the length of the field free flight tube, and $\frac{dI}{dt}$ represents the measured ToF current scaled to include the entire beam current. In other works such as [20], thrust is measured directly and only mass flow rate is calculated from the ToF data in order to estimate I_{sp}. ToF data does not include the effects of angular dispersion/transmission and energy efficiency, so thrust values obtained using equation 4.3 will be an overestimation. The calculation of mass flow rate from the ToF data measures only the emitted ion current and assumes that all mass loss is due to the emitted ions [20]. This will also lead to an overestimation in mass flow rate values.

Mass flow rate and thrust were calculated using the ToF data measured for EMIM-BF_4 and FAM-110A at emitter voltages of $\pm 1500\,V$, $\pm 1600\,V$, and $\pm 1700\,V$. Measured emitter currents at these voltages were used to account for the entire plume. Specific impulse and propulsive efficiency were then estimated for each propellant. Figure 4.19 shows the estimated thrust as a function of the emission current.

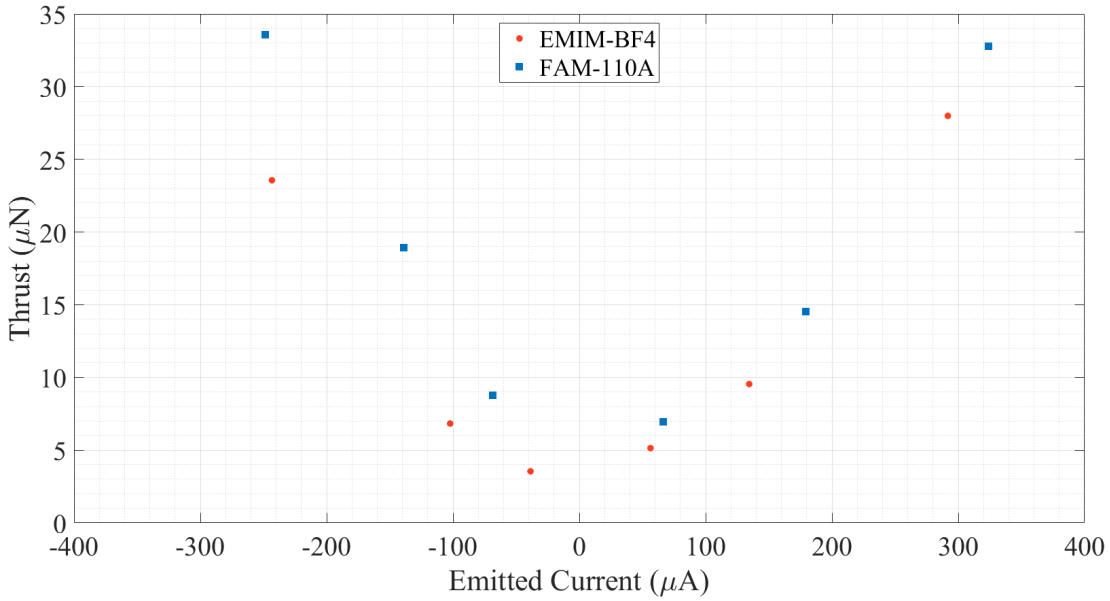

Figure 4.19: Thrust as a function emitted current

Using the above equation to calculate T_{ToF} and under the assumptions of this equation, FAM-110A has a higher predicted thrust at each emitter voltage. Thrusts of 33 μN and 34 μN were calculated at $\pm 1700\,V$. For EMIM-BF_4 thrusts of 28 μN and 24 μN were calculated at $\pm 1700\,V$. The average thrust during positive polarity was calculated as 18.1 μN and 14.2 μN for FAM-110A and EMIM-BF_4 respectively. The

average thrust calculated during negative polarity was 20.4 μN and 11.3 μN for FAM-110A and EMIM-BF_4 respectively. Using equation 4.2, the specific impulse can be calculated from the thrust and mass flow rate values predicted from the time of flight data. Figure 4.20 shows the predicted specific impulse as a function of the emitted current.

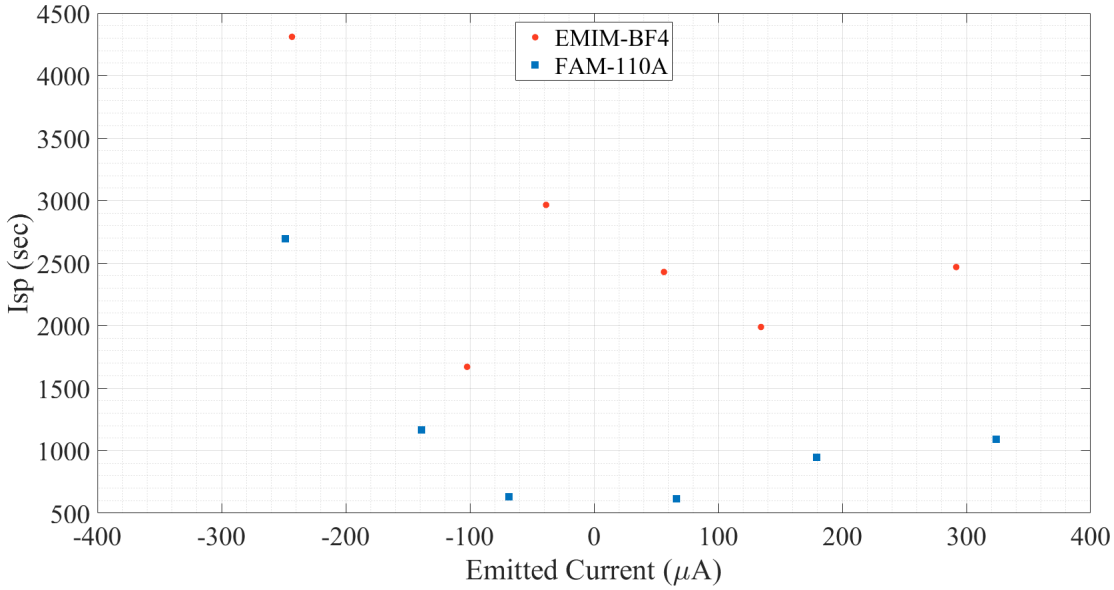

Figure 4.20: I_{sp} as a function emitted current

As expected, EMIM-BF_4 has a higher predicted specific impulse at each emitter voltage. I_{sp} values of up to 2469 seconds and 1089 seconds were calculated during positive polarity for EMIM-BF_4 and FAM-110A. During negative polarity values up to 4310 seconds and 2694 seconds were calculated for EMIM-BF_4 and FAM-110A. The average specific impulse during positive polarity was calculated as 2296 seconds for EMIM-BF_4 and 884 seconds for FAM-110A. The average specific impulse during negative polarity was 2982 seconds for EMIM-BF_4 and 1497 seconds for FAM-110A. Using the predicted thrust, mass flow rate, and specific impulse values propulsive efficiency can be calculated using equation 4.5 from [20].

$$\eta_{prop} = \frac{T_{ToF}^2}{2\dot{m}_{ToF} P_{in}} \tag{4.5}$$

Where $P_{in} = I_{emit} V_{emit}$. Average propulsive efficiencies were calculated for each propellant and are shown in Table 4.4.

Overall, FAM-110A shows a higher thrust, lower specific impulse, and lower propulsive efficiency in both emission modes when compared to EMIM-BF_4. Both propellants apear to be more efficient during

Table 4.4: Average predicted performance parameters

	Positive emission				Negative emission			
Propellant	$\dot{m}\ (\mu g/s)$	$T\ (\mu N)$	$I_{sp}\ (sec)$	$\eta_{prop}\ (\%)$	$\dot{m}\ (\mu g/s)$	$T\ (\mu N)$	$I_{sp}\ (sec)$	$\eta_{prop}\ (\%)$
EMIM-BF_4	0.62	14.2	2296	61.4	0.37	11.3	2982	81.2
FAM-110A	1.93	18.1	884	25.5	1.4	20.4	1497	60

negative emission with the calculated propulsive efficiency values and specific impulse increasing in both cases. Referring back to Tables 4.1 and 4.2, FAM-110A showed a higher average energy efficiency than EMIM-BF_4. Again, the equations used to calculated these predicted performance parameters involve a myriad of assumptions and are not necessarily accurate to values that could be measured directly. They do, however, serve as an interesting way to compare both propellants in terms of thruster performance.

Chapter 5

Conclusions

A porous glass electrospray thruster based on the design of the AFET-2 was manufactured at UIUC. Three different manufacturing techniques were explored: low speed CNC maching, laser ablation, and grinding. It was found that using a diamond edge grinding wheel produced emitters with the lowest radius of curvature, and most uniformity when compared with the other two methods. Current emission, RPA, and ToF-MS measurements were made during thruster operation with two different propellants, EMIM-BF_4 and FAM-110A. The current emission measurements with EMIM-BF_4 were comparable those presented in [13]. Currents of 770 μA and 507 μA were observed in positive and negative emission polarity. The extractor impingement fraction remained below 9% during thruster operation, higher than what was reported in [13], but most likely due to the larger measured emitter to extractor gap distance. FAM-110A emitted more current at comparable emitter voltages as compared to EMIM-BF_4. Currents of 422 μA and 305 μA were observed at voltages of +1760 V and -1730 V respectively. The extractor imipingement fraction remained below 9.5% during thruster operation. Higher impingement was observed with FAM-110A due to a 14 μm larger emitter to extractor gap. RPA measurements clearly showed $n_1 \rightarrow n_0$ fragmentation occuring in the EMIM-BF_4 plume. Less prominent fragmentation was observed in the plume of FAM-110A, with most fragmentation occuring within the acceleration region of the thruster. Energy efficiencies were calculated using the measure beam voltage for each propellant. FAM-110A showed a higher energy efficiency on average than EMIM-BF_4. The ToF data acquired for EMIM-BF_4 aligned well with that presented in [13]. The plume composition in positive emission was approximately 46% monomers, 48% dimers, and 3% trimers. In negative emission it was approximately 32% monomers, 51% dimers, and 5% trimers. In positive emission, FAM-110A showed a plume primarily consisiting of the EMIM cation. No evidence of hydroxylamine was found which is consistent with other works investigating the mass distribution of HAN based propellants [8] [19]. In negative emission,

many species were found in the plume of FAM-110A. Of the known species, nitrate and ethylsulfate were observed. Other mass to charge ratios were measured up to 200 amu/q. These other peaks in the spectra align with what was observed in [8]. Predicted performance metrics such as thrust and specific impulse were calculated for the UIUC thruster operating with each propellant. Due to assumptions within the equations, these values are predicted to be overestimates but serve as a comparison between the two propellants in terms of performance. FAM-110A shows a higher thrust, lower specific impulse, and lower propulsive efficiency in both emission modes when compared to EMIM-BF_4. Although FAM-110A shows lower efficiency and specfic impulse, it is operated as a multimode propellant whereas EMIM-BF_4 cannot operate in a chemical thruster. Overall, FAM-110A has proved iteself as an acceptable and comparable propellant in an electrospray thruster confirming its viability in a multimode propulsion system. Future work should include measured thrust values of the porous electrospray thruster operating with both propellants. This would improve the accuracy of specific impulse predictions and lead to a better comparison between the two propellants. Thruster modifications can be made to improve the variation in alignement between experiments as well as the variation in emitter to extractor gap distance.

References

[1] J. L. Rovey, C. T. Lyne, A. J. Mundahl, *et al.*, "Review of multimode space propulsion," *Progress in Aerospace Sciences*, vol. 118, Oct. 2020. DOI: 10.1016/j.paerosci.2020.100627.

[2] S. P. Berg and J. L. Rovey, "Assessment of multimode spacecraft micropropulsion systems," *Journal of Spacecraft and Rockets*, vol. 54, no. 3, 2016. DOI: 10.2514/1.A33649.

[3] C. T. Lyne, J. L. Rovey, and S. P. Berg, "Monopropellant-Electrospray Multimode Thruster Testing Results: Electrospray Mode," in *AIAA Propulsion and Energy Forum, 2021*, American Institute of Aeronautics and Astronautics (AIAA), Aug. 2021, ISBN: 9781624106118. DOI: 10.2514/6.2021-3439. [Online]. Available: https://arc.aiaa.org/doi/abs/10.2514/6.2021-3439.

[4] S. P. Berg and J. L. Rovey, "Decomposition of Double Salt Ionic Liquid Monopropellant in a Microtube for Multi-Mode Micropropulsion Applications," in *AIAA Propulsion and Energy Forum*, AIAA, 2017. DOI: 10.2514/6.2017-4755. [Online]. Available: http://arc.aiaa.org.

[5] A. Sharma, A. C. Adduci, J. L. Rovey, *et al.*, "Green Ionic Liquid Multimode Monopropellant Microthruster," *AIAA Science and Technology Forum and Exposition, AIAA SciTech Forum 2022*, pp. 1–11, 2022. DOI: 10.2514/6.2022-1733.

[6] S. P. Berg, J. L. Rovey, B. D. Prince, S. W. Miller, and R. J. Bemish, "Electrospray of an Energetic Ionic Liquid Monopropellant for Multi-Mode Micropropulsion Applications," in *AIAA Propulsion and Energy Forum*, vol. 570, AIAA, 2015, p. 3550. DOI: 10.2514/6.2015-4011. [Online]. Available: http://arc.aiaa.org.

[7] M. J. Wainwright, J. L. Rovey, S. W. Miller, B. D. Prince, and S. P. Berg, "Electrospray Mass Spectroscopy of a HAN-based Monopropellant," in *AIAA Propulsion and Energy Forum, 2018*, 2018. DOI: 10.2514/6.2018-4725. [Online]. Available: http://arc.aiaa.org.

[8] M. J. Wainwright, J. L. Rovey, S. W. Miller, B. D. Prince, and S. P. Berg, "Hydroxylammonium Nitrate Species in a Monopropellant Electrospray Plume," *Journal of Propulsion and Power*, vol. 35, no. 5, 2019. DOI: 10.2514/1.B37471. [Online]. Available: www.aiaa.org/randp..

[9] C. Coffman, "Electrically-Assisted Evaporation of Charged Fluids: Fundamental Modeling and Studies on Ionic Liquids," Ph.D. dissertation, Massachusetts Institute of Technology, 2016.

[10] C. Ma, "Design and Characterisation of Electrospray Thrusters with High Emission Density," Ph.D. dissertation, University of Southampton, 2020.

[11] D. G. Courtney, S. Dandavino, and H. Shea, "Comparing direct and indirect thrust measurements from passively fed ionic electrospray thrusters," *Journal of Propulsion and Power*, vol. 32, no. 2, pp. 392–407, 2016, ISSN: 15333876. DOI: 10.2514/1.B35836.

[12] C. Ma and C. Ryan, "Plume Characterization of a Porous Electrospray Thruster," in *36th International Electric Propulsion Conference*, 2019.

[13] M. R. Natisin, H. L. Zamora, W. A. McGehee, *et al.*, "Fabrication and characterization of a fully conventionally machined, high- performance porous-media electrospray thruster," *Journal of Micromechanics and Microengineering*, vol. 30, no. 11, p. 115 021, 2020. DOI: 10.1088/1361-6439/abb8c3.

[14] P. Lozano and M. Martínez-Sánchez, "Studies on the Ion-Droplet Mixed Regime in Colloid Thrusters," Ph.D. dissertation, Massachusetts Institute of Technology, 2003. [Online]. Available: http://ssl.mit.edu/publications/theses/PhD-2003-Lozano-TovarPaulo.pdf.

[15] C. T. Lyne, M. F. Liu, and J. L. Rovey, "A simple retarding - potential time - of - flight mass spectrometer for electrospray propulsion diagnostics," *Journal of Electric Propulsion*, 2023, ISSN: 2731-4596. DOI: 10.1007/s44205-023-00045-y. [Online]. Available: https://doi.org/10.1007/s44205-023-00045-y.

[16] S. W. Miller, J. R. Ulibarri-Sanchez, B. D. Prince, and R. J. Bemish, "Capillary ionic liquid electrospray: Beam compositional analysis by orthogonal time-of-flight mass spectrometry," *Journal of Fluid Mechanics*, vol. 928, pp. 1–32, 2021, ISSN: 14697645. DOI: 10.1017/jfm.2021.783.

[17] C. Ma, V. Messina, C. N. Ryan, *et al.*, "Plume Study of an Electrospray Thruster Using a HAN-Based Dual-Mode Ionic Liquid Propellant," in *37th International Electric Propulsion Conference*, 2022, p. 190.

[18] M. R. Klosterman, J. L. Rovey, and D. A. Levin, "Ion-induced charge emission from unpolished surfaces bombarded by an [Emim][BF4] electrospray plume," *Journal of Applied Physics*, vol. 131, no. 24, Jun. 2022, ISSN: 10897550. DOI: 10.1063/5.0060615.

[19] W. Zhou, J. Liu, S. D. Chambreau, and G. L. Vaghjiani, "Structures, proton transfer and dissociation of hydroxylammonium nitrate (HAN) revealed by electrospray ionization tandem mass spectrometry and molecular dynamics simulations," *Physical Chemistry Chemical Physics*, vol. 24, no. 22, pp. 14 033–14 043, 2022, ISSN: 14639076. DOI: 10.1039/d2cp01571d. [Online]. Available: http://dx.doi.org/10.1039/D2CP01571D.

[20] M. R. Natisin, H. L. Zamora, Z. A. Holley, *et al.*, "Efficiency mechanisms in porous-media electrospray thrusters," *Journal of Propulsion and Power*, vol. 37, no. 5, pp. 650–659, 2021, ISSN: 15333876. DOI: 10.2514/1.B38160.

Appendix A

ToF Cumulative Spectra at Other Emitter Voltages

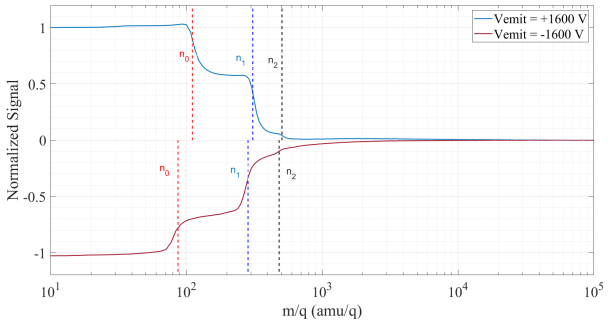

Figure A.1: EMIM-BF_4 Cumulative Mass Spectrum $\pm 1600\,V$

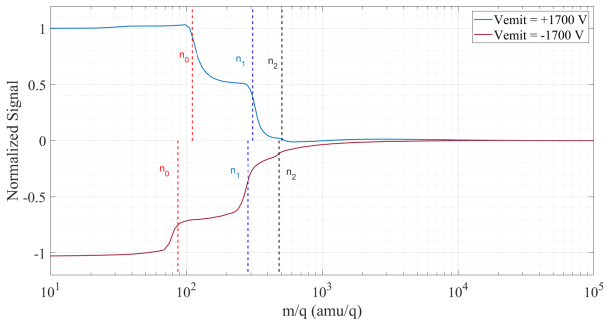

Figure A.2: EMIM-BF_4 Cumulative Mass Spectrum $\pm 1700\,V$

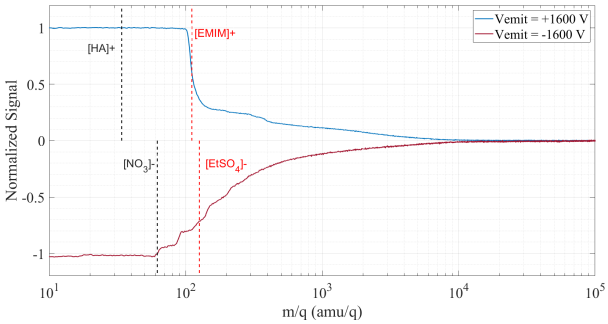

Figure A.3: FAM-110A Cumulative Mass Spectrum $\pm 1600\,V$

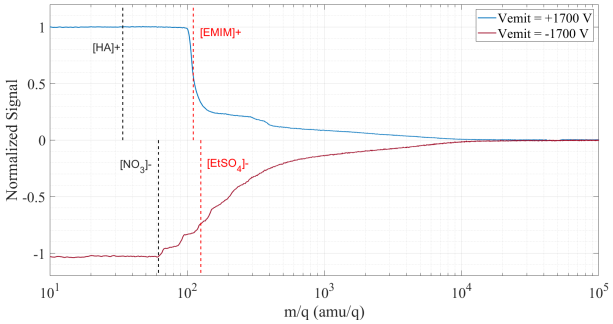

Figure A.4: FAM-110A Cumulative Mass Spectrum $\pm 1700\,V$

Appendix B

EMIM-BF_4 RPA Data

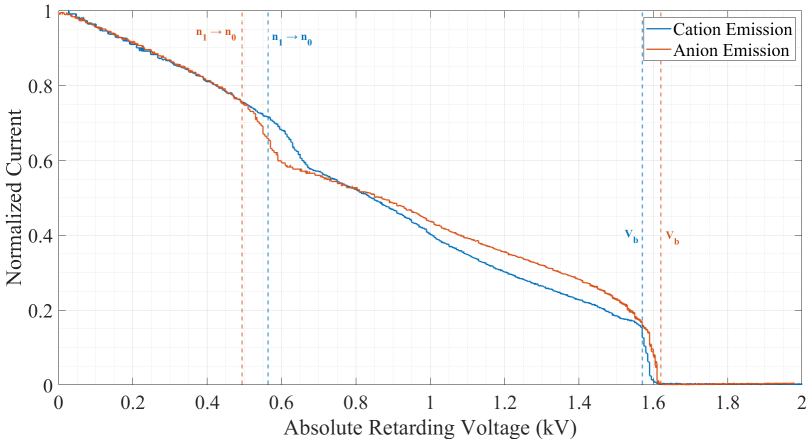

Figure B.1: EMIM-BF_4 RPA measurements, $\pm 1600\,V$

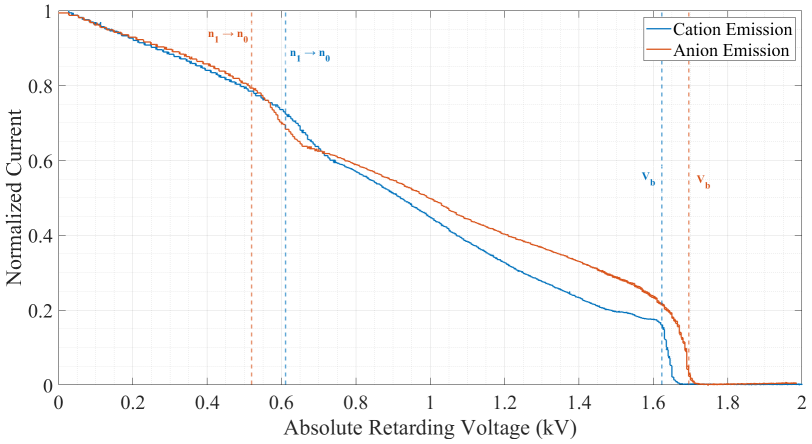

Figure B.2: EMIM-BF_4 RPA measurements, $\pm 1700\,V$

Appendix C

Thruster Testing Procedure

Day prior to electrospray test:

- Clean all parts of thruster.
  - Sonicate housing, extractor, electrode, emitter housing for 15 min, rinse with DI and IPA, desiccate for an hour.
- Assemble thruster.
  - Assemble propellant module in the following order: insert the disc spring, P4 reservoir, filter, and emitter into the center hole. Place the distal electrode over the top face of the propellant module. Carefully thread in the four bolts tightening them in star pattern until the electrode is flush with the top plane of the module and all parts are secure.
  - Place the height shim into the bottom of the aluminum housing making sure all holes are properly aligned.
  - Place the propellant module into the thruster housing and secure with four bolts inserted from the rear.
  - Place the extractor grid on the four "ledges" surrounding the propellant module. Loosely thread in the proper bolts without clamping the extractor completely.
- Align the extractor grid.
  - Place thruster in the vice making sure the thruster is parallel to the plane of the microscope.
  - Open the amscope software and focus the microscope.

  - Using the 8 set screws around the perimeter of the extractor, adjust the extractor position until a sufficient alignment is achieved. Fully tighten the four bolts to hold the extractor grid in place.

- Perform Keyence measurements.
  - Carefully place the thruster inside of a carrying case and transport it to MRL.
  - Using the Keyence, take multiple scans of the top face of the extractor grid.
  - Use these scans to measure emitter to extractor distance, and alignment.
- Use the megger to measure resistance between the emitters and the extractor/aluminum housing.
- Load thruster with propellant.
  - In the dry box, position the thruster upside down with the reservoir access hole facing up.
  - Draw the desired amount of propellant into a 1 mL syringe (amount should be ≤ 0.7 mL).
  - Place syringe on the precision balance and tare.
  - Carefully and slowly drip propellant onto the reservoir making sure the liquid does not exceed the level of the PEEK module.
  - Weigh the syringe after propellant loading and record the amount of propellant that was put into the thruster.
  - Leave the thruster upside down to allow the propellant to wick into the emitter array.

Day of electrospray test:

- Measure the resistance between the back of the reservoir and the emitter electrode to ensure propellant has wicked all the way through.
- Place thruster in desiccator and pump down. Keep under vacuum for an hour or so.
- Use the megger to measure resistance between emitter and extractor (Keep voltage to only a couple hundred volts to avoid arcing).
- Thread in the HV connection bolt. Continually measure continuity between the emitter electrode and the bolt until they are touching.
- Make correct connections to the chamber:
  - HV amp output $\rightarrow$ feedthrough 6.
  - Imoni $\rightarrow$ DAQ.

  - Vmoni → DAQ.
  - Channel 1 on signal generator 1 → Vcon-in on HV amp.
  - 50 µA range channel on back of ammeter box → feedthrough 7.
  - 50 µA range channel on front of ammeter box → DAQ.
  - Picoammeter input → feedthrough 8.
  - Make necessary ToF and RPA connections.

- Place thruster in chamber and make thruster connections:
  - Feedthrough 6 → emitter bolt.
  - Feedthrough 7 → extractor/aluminum housing.
  - Feedthrough 8 → Collector plate.

- Seal and pump down the chamber in accordance with the cross vacuum SOP.

- Perform electrospray testing:
  - Collect IV curve data for anion, cation, and bipolar emission.
  - Collect ToF Data.
  - Collect RPA Data.

Post electrospray test completion:

- Repressurize chamber in accordance with the Chris Cross vacuum SOP.

- Disconnect all thruster connections.

- Remove thruster from chamber.

- If necessary, megger the thruster. Identify anything that led to problems during testing.

- Carefully disassemble the thruster, inspecting each part and noting any observations. Look for propellant leaking, arcing to the extractor (burn marks on emitter/extractor), etc.

- Clean all components of the thruster as mentioned previously.

- Clean the emitter and reservoir by soaking in DI water, changing the water 2-3 times, then desiccating for an hour.

- Record the status of the emitter in the emitter log i.e. cracking, burns, ok, etc